Numerical investigation of the stability of bubble train flow in a square minichannel

Murat C. Öztaskin,[1,2,a)] Martin Wörner,[2,b)] and Hakan S. Soyhan[3]
[1]*Department of Mechanical Engineering, Institute of Science and Technology, University of Sakarya, 54187 Sakarya, Turkey*
[2]*Forschungszentrum Karlsruhe, Institut für Reaktorsicherheit, Postfach 3640, 76021 Karlsruhe, Germany*
[3]*Department of Mechanical Engineering, Engineering Faculty, University of Sakarya, 54187 Sakarya, Turkey*

The stability of a train of equally sized and variably spaced gas bubbles that move within a continuous wetting liquid phase through a straight square minichannel is investigated numerically by a volume-of-fluid method. The flow is laminar and cocurrent upward and driven by a pressure gradient and buoyancy. The simulations start from fluid at rest with two identical bubbles placed on the axis of the computational domain, the size of the bubbles being comparable to that of the channel. In vertical direction, periodic boundary conditions are used. These result in two liquid slugs of variable length, depending on the initial bubble-to-bubble distance. The time evolution of the length of both liquid slugs during the simulation indicates if the bubble train flow is "stable" (equal terminal length of both liquid slugs) or "unstable" (contact of both bubbles). Several cases are considered, which differ with respect to bubble size, domain size, initial bubble shape, and separation. All cases lead to axisymmetric bubbles with the capillary number in the range of 0.11–0.23. The results show that a recirculation pattern develops in the liquid slug when its length exceeds a critical value that is about 10%–20% of the channel width. If a recirculation pattern exists in both liquid slugs, then the bubble train flow is stable. When there is a recirculation pattern in one liquid slug and a bypass flow in the other, the bubble train flow may be stable or not depending on the local flow field in the liquid slugs close to the channel centerline. These results suggest that a general criterion for the stability of bubble train flow cannot be formulated in terms of the capillary and Reynolds number only, but must take into account the length of the liquid slug. ©

I. INTRODUCTION

The term "Taylor flow" refers to the flow of a sequence of elongated bubbles that move through a narrow channel and fill almost its entire cross section. Other designations frequently used in literature are slug flow, segmented flow, and bubble train flow.[1] In this paper, we will use the term "bubble train flow" since it may refer to the regular flow of trains of bubbles that are elongated (Taylor bubbles) or not, but have a diameter that is comparable to the hydraulic diameter of the channel. Bubble train flow is of interest for a number of technical applications and devices. Examples are monolith structures[2] that are traditionally used for reducing automotive emissions but are now finding increasing interest for use as multiphase monolith reactors,[3,4] microbubble columns[5] (particularly in providing extraordinary high interfacial area per unit volume), microfluidic channels,[6,7] and networks[8,9] with segmented gas-liquid flow (mainly for applications in the life sciences and microprocess engineering), and so on. From an ideal point of view, the flow in these devices should consist of bubbles of identical size and shape that move along the channel with the same axial velocity and are separated from each other by liquid slugs of uniform length. The hydrodynamics of such a perfect bubble train flow is fully described by a unit cell which consists of one bubble and one liquid slug. Perfect bubble train flow is attractive, since it would allow estimating the behavior of a single channel and the entire reactor simply by numbering up the relevant transport phenomena in a unit cell. In technical devices, however, perfect bubble train flow is hard to achieve since the generation of the individual bubbles by gas-liquid mixers, T-junctions,[10] and other devices is usually not a fully deterministic but rather a stochastic process, which may be influenced, e.g., by pressure fluctuations at the gas inlet[11] and, in general, leads to bubble size distributions.[5] For practical applications, therefore, the characteristics of the bubble train flow under variations of the size of individual bubbles and the length of liquid slugs are issues of significant importance since such variations may result in a relative motion between bubbles which might lead to coalescence. For a gas-liquid reaction in a monolith reactor or a microreactor, coalescence of bubbles is, in general, an undesired process, since it can lower the efficiency of the reactor by reducing the overall interfacial area.

For life science and lab-on-a-chip applications, the flow

[a)]LLP exchange student at University Karlsruhe and Forschungszentrum Karlsruhe. Present address: ASEP Group, Balcikkoyu, Kocagol mevkii, 41400, Gebze, Kocaeli, Turkey.
[b)]Present address: Forschungszentrum Karlsruhe, Institut für Kern- und Energietechnik, Postfach 3640, 76021 Karlsruhe, Germany.

of two immiscible liquids through a narrow channel in the form of a train of droplets is of interest. In some applications, a relative motion of adjacent drops may be of benefit since it can be utilized to direct the coalescence of drops.[12] In other applications such as for the crystallization of proteins, coalescence of drops is unwanted and gas bubbles[13] or a third immiscible liquid[14] are injected to prevent it. For the pressure driven creeping flow of neutrally buoyant drops, Ho and Leal[15] found in their experimental study in a circular capillary of 1 mm inner diameter that identical drops of comparable size that are separated by a distance more than a tube diameter exhibit identical translational velocities and interactions are negligible. This result is consistent with the analytical investigations by Hyman and Skalac.[16]

The literature on the interaction of Taylor bubbles is mainly restricted to tubes of conventional size. Moissis and Griffith[17] were the first who investigated the velocity of a Taylor bubble as it rises in a flowing liquid behind a series of other Taylor bubbles through a vertical tube. Measurements were taken for tubes with inner diameters D of 12.7, 19.05, 25.4, and 50.8 mm. The rise velocity of the trailing bubble is always larger than that of the leading one, but strongly depends on the separation distance between the bubbles, i.e., the liquid slug length L_s. For the three larger pipes, where the bubble Reynolds number is well in the turbulent zone, the experimental results for the trailing-to-leading bubble velocity ratio are well described by a decaying exponential function, which takes high values for small values of L_s and asymptotically approaches unity for very large values of L_s. For the smallest tube, the bubble Reynolds number is about 2000 and the wake effects are much shorter than for the larger tubes, since viscous effects are no longer negligible. Talvy *et al.*[18] studied the interaction between two consecutive Taylor bubbles in a stagnant liquid in a vertical pipe ($D=25$ mm). They found that even at distances exceeding 50 pipe diameters, the trailing bubble is affected by the velocity field in the wake of the leading bubble. Pinto and Campos[19] performed experiments on the interaction of two Taylor bubbles rising through stagnant liquid in vertical tubes of 19, 32, and 52 mm internal diameter and later extended their study for cocurrent liquid flow.[20] In the first study,[19] coalescence is always observed if the length of the liquid slugs is shorter than a critical distance above which there is no interaction of the bubbles. In the study for cocurrent vertical flow[20] this distance is about $5D$ if the flow is turbulent. When the liquid flow is laminar, two different situations are observed. First, if the ratio between the average velocity in the fully developed film around the bubble and the average velocity in the liquid slug is greater than 25, coalescence between bubbles is observed. The minimum distance between bubbles above which there is no interaction is about $10D$. Second, if the value of that ratio is lower than 25 and the initial distance between slugs is greater than the wake length of the leading bubble (which is about $5D$ here), then the distance between both bubbles increases during their rise and coalescence is not observed. Recently, Mayor *et al.*[21] investigated experimentally the interaction between consecutive Taylor bubbles that rise freely in the laminar regime through a vertical pipe with $D=32$ mm. They give a correlation for the ratio of velocities of the trailing and leading bubble as function of the liquid slug length. For slug length larger than $2D$ this velocity ratio is only slightly higher than 1 and approaches unity for very large values of L_s. Thus, Taylor bubbles flowing more than $2D$ apart require a long portion of the column to coalesce. However, for liquid slugs shorter than $2D$, the velocity ratio strongly increases as L_s decreases, indicating a strong interaction between both bubbles, which leads rather fast to coalescence. Thus, this correlation does reflect only the first one of the two laminar regimes observed by Pinto *et al.*[20] described above—which leads to coalescence—but not the second one where the distance between the bubbles increases and no coalescence occurs. In this context it is interesting to mention the study of Fagundes Netto *et al.*[22] who performed experiments on the bubble-bubble interaction in horizontal turbulent two-phase slug flow in a 90 m long pipe with internal diameter of 53 mm. They observed that bubbles placed behind a liquid slug smaller than a critical value move faster than the leading one, which leads to coalescence. Otherwise, they move slower than the leading one. This result is in agreement with experimental observations by Grenier[23] who found that the liquid slugs seem to interact in order to "calibrate" their length around a stable mean value, so that short slugs increase in length while longer ones decrease.

For tubes of smaller size, detailed experiments have been recently performed by Salman *et al.*[24] on the formation of Taylor bubbles in a tube of 1 mm inner diameter by a coflow tube/nozzle arrangement. They identified three mechanisms for initial bubble formation and were able to produce uniform bubble sizes for most of the cases. However, depending on the flow conditions, small non-Taylor bubbles (with diameter notably smaller than that of the tube) were formed. These non-Taylor bubbles then paired to Taylor bubbles close to the nozzle. The velocity of a small non-Taylor bubble is higher than that of a Taylor bubble because it occupies regions in the tube with higher average velocity. This eventually leads to coalescence of the trailing non-Taylor bubble with the leading Taylor bubble, increasing the size of the Taylor bubbles. By this mechanism, a wide range of bubble sizes was obtained. Almatroushi and Borhan[25] investigated experimentally the interaction and coalescence of oil drops and air bubbles rising under the action of buoyancy through a vertical tubes of 3.467 and 7.96 mm inner diameters filled with glycerol-water mixture. They consider two drops, respectively, bubbles of different sizes and report measurements of the coalescence time defined as the elapsed time between the instants of apparent contact and coalescence. The coalescence process between two bubbles can be characterized by three distinct processes. The first stage is the close approach of the two bubbles to form a thin liquid film between them, with the thickness of the liquid film being about a few microns. The second stage is film thinning or drainage, wherein the thickness of the liquid film is gradually reduced. Once the liquid film is sufficiently thin (less than about 10 nm thick), it eventually ruptures and leads to coalescence. Similar measurements, but for the coalesce time of two neutrally buoyant drops of different sizes, have already been performed before by Olbricht and co-workers[26,27] in

capillary tubes of 7 mm and 54 μm inner diameters at very low Reynolds number, $\mathrm{Re}=\mathrm{O}(10^{-2}-10^{-4})$.

Danov *et al.*[28] used a lubrication approximation to investigate analytically the effect of a surfactant on the hydrodynamic stability of a thin liquid film formed between two drops or gas bubbles, which are moving along a narrow cylindrical capillary. This study is based on the assumption that the liquid slug is very thin and is planar with a uniform thickness. This is, however, not a realistic assumption for bubble train flow where the tip of the bubble is spherical for low values of the capillary number and is pointed for larger values of the capillary number.[29,30]

Campana *et al.*[31] numerically investigated the stability of the steady motion of a liquid slug in a capillary tube by a Galerkin finite element method. The simulations are performed in a frame of reference moving with the liquid slug, which is confined between parts of two long gas bubbles. The flow in the gas phase and the gravity force are neglected. At the inlet of the computational domain, a radial velocity profile for the liquid film is prescribed. As a key result, a diagram for the uniform liquid film thickness h_∞ as function of the slug length for fixed (prescribed) values of the capillary number $\mathrm{Ca}\equiv\mu_L U_B/\sigma$ and Reynolds number $\mathrm{Re}_R \equiv \rho_L U_B R/\mu_L$ is obtained. Here, U_B is the bubble velocity, R is the tube radius, ρ_L is the density and μ_L the viscosity of the continuous liquid phase, and σ is the coefficient of surface tension. The authors use this diagram to establish whether a steady state displacement of the liquid slug is stable, i.e., the system will recover the initial state after a disturbance, or not. For example, for a capillary number $\mathrm{Ca}=0.5$ the flow is found to be hypothetically stable for Reynolds numbers $\mathrm{Re}_R=0$, 10, 20 and unstable for $\mathrm{Re}_R=40$ and 50. The authors confirm their stability map by transient calculations for hypothetically stable and unstable cases which are both found to behave as expected. In a follow-up study, Ubal *et al.*[32] determined stability charts for certain values of the Laplace number, $\mathrm{La}\equiv\rho_L\sigma R/\mu_L^2=\mathrm{Re}_R/\mathrm{Ca}$, which show the existence of a small stable region whose size increases as the Laplace number is augmented.

All the above studies concern channels with circular cross section. In circular capillaries, the liquid film thickness at the circumference of the bubble is uniform. However, microfluidic channels and channels in a monolith reactor often have rectangular cross sections. In such channels, the thickness of the liquid layer around the bubble is not uniform within a channel cross section, but is thicker in the corners of the channel. As consequence, relative motion and thus the coalescence of bubbles or drops in a train may be easier in rectangular channels than in circular capillaries. To the authors' knowledge, there exists yet no study on the stability of bubble train flow in narrow rectangular channels. In the present paper, we perform such a study for a square minichannel and numerically investigate the stability of a train of bubbles of equal size. We perform transient simulations for bubbles of two different sizes in two different flow domain sizes. The results will show that the recirculation in the liquid slug plays a critical role for stability. The organization of the paper is as follows. In Sec. II the numerical method and the computational setup are described. The results are presented in Sec. III and are discussed in Sec. IV. Conclusions are drawn in Sec. V.

II. NUMERICAL SIMULATION OF BUBBLE TRAIN FLOW

A. Governing equations and numerical method

The locally volume-averaged conservation equations for mass and momentum describing the flow of two immiscible incompressible fluids with constant material properties (density, viscosity, surface tension) can be written in the following nondimensional formulation:

$$\nabla\cdot\mathbf{v}_m=0, \tag{1}$$

$$\frac{\partial f}{\partial\theta}+\nabla\cdot f\mathbf{v}_m=0, \tag{2}$$

$$\begin{aligned}\frac{\partial(\rho_m\mathbf{v}_m)}{\partial\theta}+\nabla\cdot\rho_m\mathbf{v}_m\mathbf{v}_m&=-\nabla P+\frac{1}{\mathrm{Re}_{\mathrm{ref}}}\nabla\cdot\mu_m[\nabla\mathbf{v}_m+(\nabla\mathbf{v}_m)^T]+\frac{a_i^*\kappa^*\hat{\mathbf{n}}_i}{\mathrm{We}_{\mathrm{ref}}}\\&\quad-(1-f)\frac{\mathrm{Eo}_{\mathrm{ref}}}{\mathrm{We}_{\mathrm{ref}}}\hat{\mathbf{e}}_g+\mathrm{Fr}_{\mathrm{ref}}\hat{\mathbf{e}}_g+\frac{\mathrm{Eu}_{\mathrm{ref}}}{L^*_{\mathrm{axial}}}\hat{\mathbf{e}}_{\mathrm{axial}}.\end{aligned} \tag{3}$$

In the above equations, ρ_m is the nondimensional mixture density given by

$$\rho_m\equiv\frac{f\rho_L+(1-f)\rho_G}{\rho_L}, \tag{4}$$

μ_m is the nondimensional mixture viscosity given by

$$\mu_m\equiv\frac{f\mu_L+(1-f)\mu_G}{\mu_L}, \tag{5}$$

$\mathbf{v}_m$ is the nondimensional center-of-mass velocity given by

$$\mathbf{v}_m\equiv\frac{1}{U_{\mathrm{ref}}}\frac{f\rho_L\overline{\mathbf{v}_L}^L+(1-f)\rho_G\overline{\mathbf{v}_G}^G}{f\rho_L+(1-f)\rho_G} \tag{6}$$

and f is the local liquid volumetric fraction within the averaging volume. In our computations, a regular rectilinear grid of uniform size is used and the averaging volume is taken to be the volume of a mesh cell. Therefore, we have $f=1$ for liquid filled cells and $f=0$ for gas filled cells while f may take any value between 0 and 1 for interface cells. In Eq. (6), $\overline{\mathbf{v}_L}^L$ and $\overline{\mathbf{v}_G}^G$ are the intrinsic mean velocities averaged over the volume of the respective phase within the mesh cell. In the set of Eqs. (1)–(3) it has been already assumed that in interface mesh cells there is no the relative velocity between the phases, i.e., $\mathbf{v}_r\equiv\overline{\mathbf{v}_G}^G-\overline{\mathbf{v}_L}^L=0$. This corresponds to a locally homogeneous model. Therefore, the terms depending on $\mathbf{v}_r$ in the general volume-averaged equations have been neglected.

For normalization of the governing equations, a reference length scale L_{ref} and a reference velocity scale U_{ref} are used. Therefore, in the nondimensional Navier–Stokes equation (3), several nondimensional numbers based on reference scales appear. The definitions of the reference Reynolds

number, reference Weber number, reference Eotvos number, reference Froude number, and reference Euler number are

$$\mathrm{Re}_{\mathrm{ref}} \equiv \frac{\rho_L L_{\mathrm{ref}} U_{\mathrm{ref}}}{\mu_L}, \tag{7}$$

$$\mathrm{We}_{\mathrm{ref}} \equiv \frac{\rho_L L_{\mathrm{ref}} U_{\mathrm{ref}}^2}{\sigma}, \tag{8}$$

$$\mathrm{Eo}_{\mathrm{ref}} \equiv \frac{(\rho_L - \rho_G) g L_{\mathrm{ref}}^2}{\sigma}, \tag{9}$$

$$\mathrm{Fr}_{\mathrm{ref}} \equiv \frac{g L_{\mathrm{ref}}}{U_{\mathrm{ref}}^2}, \tag{10}$$

$$\mathrm{Eu}_{\mathrm{ref}} \equiv \frac{\overline{p_0} - \overline{p}_{L_{\mathrm{axial}}}}{\rho_L U_{\mathrm{ref}}^2}. \tag{11}$$

In Eqs. (2) and (3), θ is the nondimensional time,

$$\theta \equiv \frac{t}{t_{\mathrm{ref}}} = t \frac{U_{\mathrm{ref}}}{L_{\mathrm{ref}}}, \tag{12}$$

while in the surface tension term of Eq. (3), σ is the coefficient of surface tension, $\hat{\mathbf{n}}_i$ is the unit normal vector to the interface pointing into the liquid phase, $a_i^* \equiv a_i L_{\mathrm{ref}}$ denotes the nondimensional volumetric interfacial area concentration, and $\kappa^* \equiv \kappa L_{\mathrm{ref}}$ is twice the nondimensional mean interface curvature. Here, the superscript " *" is used to distinguish a nondimensional quantity from its dimensional counterpart.

Since the single-field Navier–Stokes equation (3) shall be applicable to a domain with periodic boundary conditions, the dimensionless "reduced pressure" P has been introduced, which is related to the dimensional physical pressure p via

$$P \equiv \frac{1}{\rho_L U_{\mathrm{ref}}^2} \left(p + \frac{\overline{p_0} - \overline{p}_{L_{\mathrm{axial}}}}{L_{\mathrm{axial}}} \hat{\mathbf{e}}_{\mathrm{axial}} \cdot \mathbf{x} \right). \tag{13}$$

Here, $\overline{p_0}$ is the plane average of p over the cross section at $\mathbf{x}=0$ while $\overline{p}_{L_{\mathrm{axial}}}$ is the plane average over the cross section at $\mathbf{x}=L_{\mathrm{axial}}\hat{\mathbf{e}}_{\mathrm{axial}}$ and $\hat{\mathbf{e}}_{\mathrm{axial}}$ is the unit normal vector in axial direction. In the above equations, furthermore, $\mathbf{g}=g\hat{\mathbf{e}}_g$ is the gravity vector ($g=9.81\ \mathrm{m/s^2}$), and $L_{\mathrm{axial}}^* \equiv L_{\mathrm{axial}}/L_{\mathrm{ref}}$ is the nondimensional axial length of the computational domain.

The above equations are implemented in our in-house computer code TURBIT-VOF.[33,34] The code is based on a finite volume method and employs a regular Cartesian staggered grid, which is uniform in the x- and y-directions and optionally nonuniform in z-direction. In this paragraph we give only a short summary of the numerical method and refer to Appendix for details. The strategy to solve Eqs. (1) and (3) involves a projection method where the resulting Poisson equation is solved by a conjugate gradient method. For time integration of the momentum equation (3) an explicit third order Runge–Kutta scheme is employed. All spatial derivatives are approximated by second order central difference schemes. The volume fraction advection equation (2) is solved by means of a volume-of-fluid (VOF) method with interface reconstruction. The interface is locally approximated as a plane whose orientation and location within a mesh cell are determined by the exact plane interface reconstruction algorithm[33] (EPIRA). In the unsplit advection step of the VOF procedure the fluxes of liquid over the cell faces are computed in a geometrical manner. The code has been verified by a number of test problems[33] (e.g., capillary waves, gravity waves, Rayleigh–Taylor instability) and has been applied to different bubbly flows.[34–36] In a computational exercise, Özkan *et al.*[37] compared the performance of the VOF method in the TURBIT-VOF code for bubble train flow in a square minichannel with that of three commercial computational fluid dynamics (CFD) codes. It is found that the results of the two codes with state-of-the art piecewise-linear interface reconstruction, TURBIT-VOF and FLUENT, are in good agreement and are clearly superior to codes which use no interface reconstruction to solve the volume fraction advection equation but use difference schemes instead. Recently, the code has also been validated for cocurrent downward Taylor flow in a viscous liquid, where the computed bubble shape was in good agreement with experimental flow visualizations for a wide range of capillary numbers.[38]

B. Validation by Bretherton's problem

For further validation of the code we perform simulations of the pressure driven flow of long bubbles in a plane horizontal channel and compare the results with asymptotic results of the two-dimensional (2D) Bretherton problem.[39] The latter is given by the steady movement of an inviscid gas between two closely spaced parallel plates separated a distance $2d$, displacing an incompressible Newtonian liquid of constant viscosity and density. The semi-infinite gas bubble is translating steadily with speed U_B and leaves behind a thin liquid film. The thickness of this film is

$$\frac{h_{\mathrm{film}}}{d} = 1.3375\mathrm{Ca}^{2/3}. \tag{14}$$

Giavedoni and Saita[40] performed a computational study of the Bretherton problem and found that their results match this theoretical correlation for $\mathrm{Ca} < 10^{-3}$, while for larger capillary numbers there is a significant deviation from it. Halpern and Gaver[41] performed a boundary element analysis of the 2D Bretherton problem and obtained by a regression analysis of the numerical results the relation

$$\frac{h_{\mathrm{film}}}{d} = 0.417 \exp(-1.69\mathrm{Ca}^{0.5025}), \tag{15}$$

which is valid for capillary numbers in the range of $0.05 \leq \mathrm{Ca} \leq 100$.

Since our three-dimensional (3D) code does not allow the consideration of a semi-infinite and inviscid bubble, we approximate the 2D Bretherton problem as follows. We consider two rigid planes with no-slip boundary conditions separated by a distance $2d=1$ mm. In axial direction, the size of the computational domain is $20d$ and the boundary conditions are periodic. We also use periodic boundary conditions in spanwise direction. However, the extension of the computational domain in span-wise direction is very small and the number of mesh cells is only 4. Therefore, there is a very

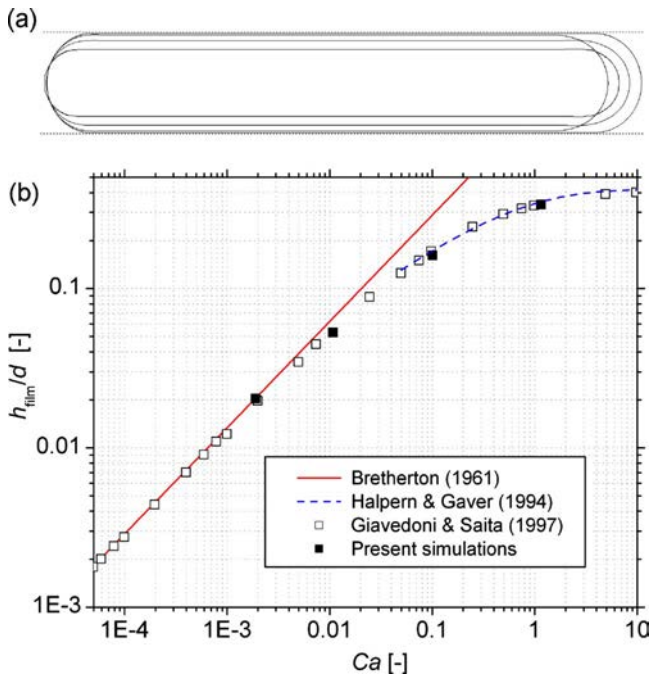

FIG. 1. (Color online) (a) Computed steady bubble shape for the four different capillary numbers. The dashed lines denote the channel walls. The flow is from left to right. (b) Comparison of computed liquid film thickness (filled squares) with the correlation of Bretherton (Ref. 39) (solid line), the numerical results of Giavedoni and Saita (Ref. 40) (open squares), and the correlation of Halpern and Gaver (Ref. 41) (dashed line).

strong coupling in spanwise direction, and although the simulations are performed in 3D, the numerical results show no variations in spanwise direction. In this computational domain we place a plane bubble with hemispherical ends and a length of about $10d$. We neglect gravity and start the simulation from a laminar velocity profile with a mean velocity of about 1 mm/s and a prescribed axial pressure drop of about 0.5–0.7 Pa. The simulation is continued until constant values are obtained for the mean axial gas and liquid velocity. The viscosity of the liquid is $\mu_L = 0.01$ Pa s while that of the gas is $\mu_G = 10^{-5}$ Pa s. Both values result in a viscosity ratio $\mu_G/\mu_L = 0.001$, which is small so that we can compare our results with those for an inviscid bubble. We consider four cases with different values of the coefficient of surface tension, which is in the range of $10^{-5} - 4 \times 10^{-3}$ N/m. These parameters result in four distinct values of the capillary number within the range of 0.0019–1.15. Since these simulations are very time consuming, we consider the artificial case where the density of both phases is equal, namely, $\rho_L = \rho_G = 1000$ kg/m^3, so that we can use an efficient direct solver for the pressure Poisson equation. For all four cases the value of the bubble Reynolds number is in the order of 0.1. Thus, inertial effects should be negligible. For all four cases we use a uniform grid, which consists of $1000 \times 4 \times 100$, $1600 \times 4 \times 160$, and $2000 \times 4 \times 200$ mesh cells, respectively. Figure 1(a) shows a comparison of the computed steady bubble shapes for the four different cases. A comparison of the computed liquid film thickness with Eqs. (14) and (15) and the numerical results of Giavedoni and Saita[40] is displayed in Fig. 1(b) and shows good agreement.

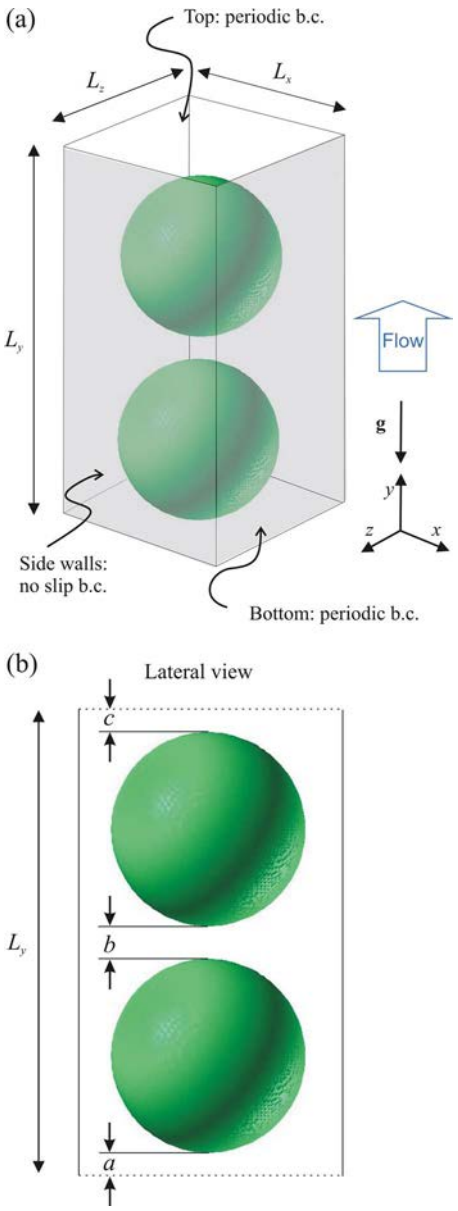

FIG. 2. (Color online) Sketch of computational domain, boundary conditions, and initial bubble positions. (a) Perspective view; (b) lateral view.

C. Computational setup and test cases for bubble train flow

In this paper, we perform computations of the cocurrent upward bubble train flow in a square vertical channel in a fixed frame of reference. Figure 2(a) shows a sketch of the coordinate system and the computational domain. We denote the horizontal directions by x and z and the vertical direction by y. The horizontal dimensions of the computational domain are $L_x = L_z = D_h = L_{\text{ref}} = 2$ mm. At the four sidewalls no-slip boundary conditions apply, while in vertical direction periodic boundaries are used at the top ($y = L_y$) and bottom ($y = 0$) of the computational domain. While in a previous study[36] a single unit cell with one bubble and one liquid slug was considered, in the present study two bubbles are placed within the computational domain. Three basic cases are considered. For each case a number of simulations are performed. For case A the height of the channel is $L_y = L_{\text{axial}}$

TABLE I. Summary of parameters and results of the different simulations. The values for U_L, U_G, and J correspond to the last time step of the transient simulations.

Case	Domain	Grid	Time steps	ε	D_B^0/D_h	L_B^0/D_h	L_{s1}^0/D_h	L_{s2}^0/D_h	$\lambda=L_{s2}^0/L_{s1}^0$	U_L/U_{ref}	U_G/U_{ref}	J/U_{ref}
A1	$1\times2\times1$	$48\times96\times48$	50 000	33.07	0.858	0.858	0.142	0.142	1	1.20	3.66	2.02
A2	$1\times2\times1$	$48\times96\times48$	200 000	33.07	0.858	0.858	0.152	0.132	0.87	1.20	3.64	2.01
A3	$1\times2\times1$	$48\times96\times48$	11 200	33.07	0.858	0.858	0.192	0.092	0.48	1.17	3.58	1.97
A4	$1\times2\times1$	$48\times96\times48$	57 200	33.07	0.808	0.944	0.066	0.046	0.70	1.20	3.66	2.02
A0g	$1\times2\times1$	$48\times96\times48$	130 000	33.07	0.858	0.858	0.192	0.092	0.48	0.80	1.92	1.17
B1	$1\times3\times1$	$48\times144\times48$	70 000	33.03	0.848	1.227	0.274	0.274	1	1.37	3.96	2.22
B2	$1\times3\times1$	$48\times144\times48$	100 000	33.03	0.848	1.227	0.324	0.224	0.69	1.37	3.96	2.22
B3	$1\times3\times1$	$48\times144\times48$	150 000	33.03	0.848	1.227	0.364	0.184	0.51	1.37	3.96	2.22
B4	$1\times3\times1$	$48\times144\times48$	140 000	33.03	0.848	1.227	0.464	0.084	0.18	1.37	3.96	2.22
C1	$1\times3\times1$	$48\times144\times48$	70 000	22.05	0.858	0.858	0.856	0.428	0.5	1.23	2.79	1.57
C2	$1\times3\times1$	$48\times144\times48$	17 200	22.05	0.858	0.858	0.092	1.192	0.077	1.22	2.78	1.57

$=4$ mm, while for cases B and C it is $L_y=L_{\mathrm{axial}}=6$ mm. Thus, the nondimensional size of the computational domain in terms of L_{ref} is $1\times2\times1$ for case A and is $1\times3\times1$ for cases B and C.

As initial conditions, two equal-sized axisymmetric bubbles are placed within the computational domain. Bubbles of two different volumes are considered. For the small bubble, the volume-equivalent diameter is $D_{\mathrm{eq}}/D_h=0.858$, while for the large bubble it is $D_{\mathrm{eq}}/D_h=0.982$. The initial shape of the large bubble is elongated (Taylor bubble like) with a bubble length of $L_B^0/D_h=1.227$ and bubble diameter $D_B^0/D_h=0.848$. For the small bubble, the initial shape may be either spherical ($D_B^0=D_{\mathrm{eq}}$) or elongated ($L_B^0/D_h=0.944$, $D_B^0/D_h=0.808$). In most of the simulations the void fraction within the computational domain is $\varepsilon\approx33\%$ (cases A and B) while two simulations are performed for $\varepsilon\approx22\%$ (case C). The two bubbles are place in line on the centerline of the channel as illustrated in Fig. 2(b). Due to the periodic boundary conditions in axial direction, this configuration corresponds to two liquid slugs of initial length $L_{s1}^0=b$ and $L_{s2}^0=a+c$. To investigate the stability of the bubble train flow, we perform simulations for different values of the initial liquid slug length ratio $\lambda\equiv(a+c)/b$.

The physical properties of the fluids are the same as in a previous study.[36] The liquid density $\rho_L=957\ \mathrm{kg/m^3}$ and viscosity $\mu_L=0.048$ Pa s are representative for one of the silicon oils used in the experiments of Thulasidas *et al.*[1] For the gas phase we use $\rho_G=11.7\ \mathrm{kg/m^3}$ and $\mu_G=0.184$ mPa s, both values being ten times larger than those for air. It has been shown that this increase in the gas density and viscosity has a negligible effect on the bubble velocity and bubble shape but allows for a significant saving of CPU time since much larger time steps can be used.[36] The value of the coefficient of surface tension is $\sigma=0.022\ 18\ \mathrm{N/m}$. For the reference velocity we use $U_{\mathrm{ref}}=0.0264\ \mathrm{m/s}$. The reference time scale then becomes $t_{\mathrm{ref}}=0.075$ s.

In our simulations we do not—due to the periodic boundary conditions—prescribe the phase volumetric flow rates but specify the pressure drop across the computational domain. Here, we have $\hat{\mathbf{e}}_{\mathrm{axial}}=-\hat{\mathbf{e}}_g=\hat{\mathbf{e}}_y$ and can combine the last two source terms in Eq. (3) as

$$\mathrm{Fr}_{\mathrm{ref}}\hat{\mathbf{e}}_g+\frac{\mathrm{Eu}_{\mathrm{ref}}}{L^*_{\mathrm{axial}}}\hat{\mathbf{e}}_{\mathrm{axial}}=\left(\frac{\mathrm{Eu}_{\mathrm{ref}}}{L^*_{\mathrm{axial}}}-\mathrm{Fr}_{\mathrm{ref}}\right)\hat{\mathbf{e}}_y=\Pi\hat{\mathbf{e}}_y. \tag{16}$$

In all present simulations we use $\Pi=27.03$. This corresponds to a pressure difference $(\overline{p_0}-\overline{p_{L_{\mathrm{axial}}}})=73.6$ Pa for case A and $(\overline{p_0}-\overline{p_{L_{\mathrm{axial}}}})=110.4$ Pa for cases B and C. In addition to this source term, the flow is driven by buoyancy. Only for case A0g we set $g=0$. Having specified the driving forces, the volumetric flow rates of the phases, Q_G and Q_L, adjust accordingly within the transient simulation. The total superficial velocity is then given by $J=(Q_G+Q_L)/A_{\mathrm{ch}}=\varepsilon U_G+(1-\varepsilon)U_L$, where A_{ch} is the cross-sectional area of the channel and U_G and U_L denote the mean velocities of the phases.

Table I gives an overview on all simulation runs of the present study. In all simulations the grid is rectilinear, uniform, and isotropic and a mesh size $h/L_{\mathrm{ref}}=1/48$ is used. A grid refinement study has demonstrated that this resolution is sufficient.[36] For most of the cases the time step width is $\Delta t/t_{\mathrm{ref}}=2.5\times10^{-5}$; only for case A2 it is 10^{-5}. For our previous simulations with similar physical and numerical parameters, a validation by experimental data[1] has been performed and showed good agreement.[36]

III. STABILITY OF BUBBLE TRAIN FLOW

In the present paper we are interested only in the first stage of a possible coalescence process, i.e., the close approach of the two bubbles. This is because in the current implementation of our fixed-grid VOF method, we cannot reliably describe the thinning and rupture of the film separating the trailing and the leading bubble when the length of the liquid slug becomes less than one mesh cell. To evaluate if the bubble train flow is "stable" or not, we consider the time evolution of the length of both liquid slugs within each simulation. If, during the course of the simulation, the length of the longer slug will decrease and that of the short slug will

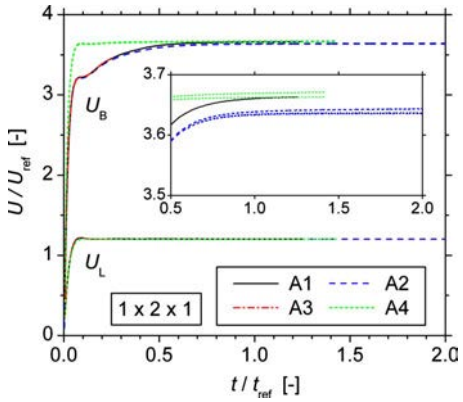

FIG. 3. (Color online) Time history of the mean liquid velocity U_L and the velocity U_B of the two bubbles for the different runs of case A.

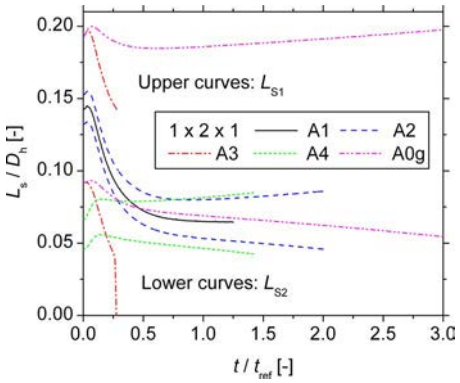

FIG. 5. (Color online) Time history of the slug lengths L_{S1} and L_{S2} for the different runs of case A.

increase, then eventually both liquid slugs will have the same length and we can argue that the bubble train flow is stable. On the other hand, it is "unstable" if the length of the shorter liquid slug continues to decrease until it finally becomes zero when the bubbles are in contact. In the sequel, we will denote this close approach and contact of the two bubbles as "coagulation." In practical applications, the coagulation may lead or may not lead to coalescence of the bubbles, depending on the presence of surfactants and the intermolecular interactions between the bubble surfaces. In the following, we first discuss the time evolution of the bubble velocities and then that of the liquid slug length, since a change in the length of the liquid slugs will only occur if the velocity of both bubbles is different.

A. Time evolution of bubble velocities and mean liquid velocity

In Fig. 3 we show the time history of the velocity of both bubbles and that of the mean liquid velocity within the computational domain, U_L, for the different runs of case A. Figure 4 shows the same but for case B. We find that for all runs of case A the terminal mean liquid velocity is the same. The same holds for all runs of case B. Comparing the time evolution of U_L for cases A1 and A4, we find that the initial shape of the two bubbles—which is spherical for case A1 and is elongated for case A4—influences the initial phase of the simulation where the bubbles accelerate from rest. However, the initial bubble shape is without influence on the terminal value of U_L. As concerns the velocity of the two bubbles, we find that these are identical in case A1 and in case B1 where the initial length of both slugs is the same. However, the inset graphics in Figs. 3 and 4 shows that the terminal velocities of the two bubbles slightly differ for all those cases where the initial length of the liquid slugs is different. From Fig. 3 we observe that the bubble reaches a velocity close to its terminal one much faster, when its initial shape is elongated (case A4) than when it is spherical (cases A1–A3). Using the terminal bubble velocity to estimate the bubble Reynolds number and the capillary number, we obtain for case A1 $\mathrm{Re}_B \equiv \rho_L U_B D_h / \mu_L = 3.86$ and $\mathrm{Ca} \equiv \mu_L U_B / \sigma = 0.21$, and for case B1 $\mathrm{Re}_B = 4.17$ and $\mathrm{Ca} = 0.23$.

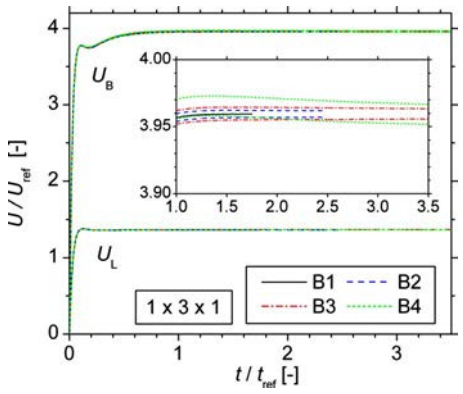

FIG. 4. (Color online) Time history of the mean liquid velocity U_L and the velocity U_B of the two bubbles for the different runs of case B.

B. Time evolution of liquid slug length

From the time evolution of the translational velocity of both bubbles as displayed in Figs. 3 and 4 alone, we cannot judge if there will be finally coagulation or not. This is because the relative velocity between the bubbles may result in one of two situations. In the first one, the length of the longer slug may further increase in time while that of the shorter slug further decreases; a situation that will finally lead to coagulation. In the second possible case, the length of the longer slug may decrease in time while that of the shorter slug increases; a situation that finally leads to slugs of equal length, i.e., stable bubble train flow. Therefore, in this section we discuss the time evolution of the length of both liquid slugs.

We begin with the simulation results for case A (domain $1 \times 2 \times 1$) which are displayed in Fig. 5. For case A1, where the initial length of both slugs is the same ($\lambda = 1$), the length of both liquid slugs stays equal during the entire simulation, though, the liquid slug length first decreases in time but eventually approaches a constant value. This decrease in the liquid slug length in the first part of the simulation corresponds with the elongation of the initially spherical bubbles. After this transient, both bubbles obey a steady shape and thus constant liquid slug lengths are obtained. The time needed by the bubbles to complete the deformation from the initial shape toward the steady shape can be identified for each cases from the time evolution of the sum of the length

of both liquid slugs. For all runs of cases A and B the bubble deformation is finished at $t/t_{ref} \approx 1$. For cases A2–A4 and A0g, the initial lengths of the liquid slugs are different while the sum of the initial length of both slugs is the same for all cases. The initial slug length ratio is $\lambda = 0.87$ for case A2, is $\lambda = 0.48$ for case A3 and A0g, and is $\lambda = 0.3$ for case A4. As λ decreases, the length of one of the liquid slugs becomes shorter, enhancing the possibility for coagulation. For case A3 we see in Fig. 5 that the length of the short slug strongly decreases in time. At $t/t_{ref} \approx 0.26$ the slope of the curve changes and the slug length rapidly approaches zero, indicating coagulation of the two bubbles. When the distance between the two bubbles is less than two mesh cells, their interfaces lie in adjacent mesh cells. Since our VOF method does not distinguish between fractional volumes of individual bubbles, the interface reconstruction algorithm may fail and can lead to artificial coalescence of the bubbles. In the present computations the nondimensional grid size in terms of the hydraulic diameter is $1/48 = 0.021$. The kink that is seen in Fig. 5 for the shorter liquid slug of case A3 can be explained by this artificial coalescence and should not be taken to be physical. However, the conclusion that coagulation occurs for case A3 remains unaffected. For case A2 we observe that the length of the long slug first decreases in time but then continuously increases for $t/t_{ref} > 0.8$, when the deformation of the initial spherical bubble to an elongated shape is established. For the length of the shorter liquid slug, we observe a continuous decrease. For $t/t_{ref} > 1$ the slope of the individual curves in Fig. 5 is about constant in time. With this observation and because the bubble shape is steady for $t/t_{ref} > 1$, we make the assumption that the curves in Fig. 5 can be extrapolated to larger times. This suggests that for case A2 finally coagulation will occur. However, this conjecture cannot be proven since the simulation is not continued until coagulation because the approach of the two bubbles is rather slow and would require a prohibitively large amount of additional CPU time.

In order to investigate if the initial bubble shape has an influence whether coagulation occurs or not, we perform one simulation, case A4, which is not started from spherical bubbles (as cases A1–A3 and A0g) but from elongated bubbles of the same volume. Figure 5 shows that not only for cases A2 and A3 but also for case A4 coagulation occurs, regardless of the initial bubble shape. We remark, however, that for the confined motion of a single drop through a cylindrical capillary, the breakup behavior strongly depends on the initial drop shape as shown by the computations of Johnson and Borhan.[42]

Of interest is also the influence of the buoyancy force. Therefore, for case A0g the gravitational acceleration g has been set to zero so that in this case the flow is driven by the pressure gradient only. The ratio of the magnitude of the driving forces buoyancy to pressure is given by $Eo_{ref}/(We_{ref}\Pi)$ and takes a value of 1.03 for cases A1–A4. The total driving force experienced by the bubble is thus about 49% lower for case A0g than for cases A1–A4, while the driving force experienced by the liquid is the same. As a consequence, the terminal liquid velocity of case A0g is about 34% lower than for case A1, while the terminal velocity of the bubbles and thus the capillary number is about 48% lower. The lower value of Ca for case A0g is associated with a larger bubble diameter and shorter bubble length, resulting in longer liquid slugs. The time evolution of the length of both liquid slugs for case A0g is shown in Fig. 5. They indicate that the bubble train flow is unstable, too. Thus, we conclude that the stability of bubble train flow is not sensitive to the buoyancy force (at least for the hydrodynamic parameters investigated here) but is mainly related to the driving pressure force.

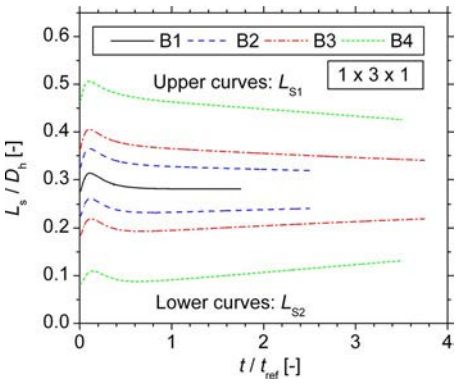

FIG. 6. (Color online) Time history of the slug lengths L_{S1} and L_{S2} for the different runs of case B.

Figure 6 shows the time evolution of the length of the two liquid slugs for the runs of case B, i.e., for the computational domain of nondimensional size of $1 \times 3 \times 1$. For case B1 with equal initial slug length ($\lambda = 1$) we find—similar to case A1—that the lengths of both liquid slugs stay equal throughout the simulation. However, since in case B1 the initial bubble shape is not spherical but elongated, we observe in Fig. 6 first an increase in the length of both liquid slugs and then a decrease until eventually constant values are obtained. For cases B2–B4, the initial length of the liquid slugs is different, see Table I. For all these cases, we observe that for $t/t_{ref} > 0.6$ the shorter liquid slug gets longer and the longer liquid slug gets shorter. Although not explicitly demonstrated, as the simulations are not continued, it is likely that this change in lengths of both liquid slugs remains until finally their length is equal, and so are the translational velocities of both bubbles. Thus, cases B2–B4 tend to the terminal behavior of case B1. In this sense, the bubble train flow of case B is stable.

In summary, we find that all runs of case A where the initial slug length ratio λ differs from unity are unstable, i.e., lead to coagulation, while all runs of case B are stable. It is interesting to note that for $\lambda < 1$ the actual value of λ has—for the range of λ studied here—neither for case A nor for case B an influence if coagulation occurs or not. It has, however, of course an influence on the time that elapses until either coagulation occurs or equal slug lengths are established. For case A2 where λ is close to unity it takes very long until coagulation occurs, while for case B4 where λ is close to zero it takes very long until equal slug lengths are obtained.

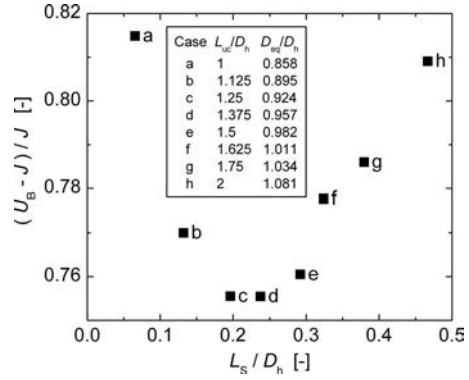

FIG. 7. Nondimensional relative velocity as function of the nondimensional slug length evaluated from the simulation results of Wörner *et al.* (Ref. 36).

IV. DISCUSSION

In Sec. III we observed that—for the same driving forces and same gas hold-up in the unit cell—the bubble train flow in the domain of nondimensional size $1\times2\times1$ is unstable (case A) while it is stable in domain $1\times3\times1$ (case B). The reason for this behavior is discussed in this section. It is obvious that this behavior may have its origin in the main differences between both cases, which are the different liquid slug lengths and different bubble sizes. We therefore investigate next the dependence of the relative bubble velocity on both parameters.

A. Dependence of relative velocity on liquid slug length

The stability of ideal bubble train flow may be related to the dependence of the nondimensional relative velocity on the length of the liquid slug. To the authors knowledge there is yet no information available in literature how for a perfect bubble train flow $W\equiv(U_B-J)/U_B$ or $Z\equiv(U_B-J)/J$ depend on L_s/D_h for bubbles of various sizes D_{eq}/D_h. However, in our previous numerical study[36] we investigated, for one bubble within the axially periodic domain, the influence of the length of the unit cell on different hydrodynamic parameters. In these simulations, which we denote here by cases a–h, the unit cell length takes eight distinct values in the range of $1\leq L_{\mathrm{uc}}/D_h\leq2$. For all cases, the void fraction is the same, $\varepsilon=33\%$, to ensure that the buoyancy force per unit volume is the same. Thus, the bubble volume increases from case "a" to "h" and is in case "h" twice that of case "a." In addition, the second driving force, i.e., the prescribed pressure gradient per unit length, is the same for all cases a–h. An interesting result of this study[36] was that the nondimensional relative velocity $W\equiv(U_B-J)/U_B$ displayed as function of the capillary number shows a local minimum [see Fig. 4(c) of Wörner *et al.*[36]], since for short unit cell length W decreases with Ca while for long unit cell length it increases. The latter is consistent with theoretical studies[29,39,43] and experimental results for long bubbles, where a monotonic increase in W with increasing value of Ca is found both for circular channels[1,44–46] and for square channels.[1]

In Fig. 7 we display the results of the numerical study of Wörner *et al.*[36] in a different form, namely, $Z\equiv(U_B-J)/J$ as function of the liquid slug length. The lower case characters a–h indicate the cases with different unit cell lengths. Figure 7 shows a local minimum. The present case A corresponds to case "a" and the present case B corresponds to case "e." Therefore, the present cases A and B are in different branches of the virtual curve shown in Fig. 7. If we assume that the bubble velocity mainly depends on the length of the liquid slug ahead of it (as indicated by the experimental results discussed in Sec. I), then we can use Fig. 7 to estimate what happens if one disturbs an ideal bubble train flow where all liquid slugs have the same length L_s^{eq}. We thus virtually decrease the length of the liquid slug in front of a "leading" bubble $L_s^{\mathrm{lead}}=L_s^{\mathrm{eq}}-\delta L_s$ by a small amount δL_s, and at the same time increase the length of the liquid slug of the neighboring trailing bubble by the same amount so that $L_s^{\mathrm{trail}}=L_s^{\mathrm{eq}}+\delta L_s$. For case A, respectively, "a," the relative velocity between the leading bubble and the total superficial velocity J increases, while the relative velocity of the trailing bubble with respect to J decreases. Thus, the slug length L_s^{lead} ahead of the leading bubble will further decrease while that ahead of the trailing bubble, L_s^{trail}, will further increase. This will finally lead to coagulation, so that the bubble train flow in this branch is unstable. On the other hand, for case B, respectively "e," Fig. 7 shows that the leading bubble with liquid slug length $L_s^{\mathrm{lead}}=L_s^{\mathrm{eq}}-\delta L_s$ ahead of it will slow down compared to J, while at the same time the relative velocity of the trailing bubble with liquid slug length $L_s^{\mathrm{trail}}=L_s^{\mathrm{eq}}+\delta L_s$ ahead of it will increase. As time advances, this change in the relative velocity of both bubbles results in an increase in the length of the shorter liquid slug, L_s^{lead}, and a decrease in the length of the longer liquid slug L_s^{trail}. Thus, we may expect that the disturbance will diminish with time and finally the length of both liquid slugs is the same and is equal to L_s^{eq}. For this situation, therefore, the bubble train flow is stable.

At this point, it is appropriate to sound a note of caution. As already mentioned, the simulations for cases a–h in Fig. 7 correspond to bubbles of different sizes while the magnitude of the driving forces is kept constant. In the present simulations, however, the size of the two bubbles is the same, both experiencing the same driving forces. Nevertheless, Fig. 7 is helpful to explain the unstable behavior found for simulations of present cases A and the stable behavior of present cases B. To explain the nonmonotonic hydrodynamic behavior of cases a–h in Fig. 7, we investigate next the dependence of the nondimensional relative velocity $Z\equiv(U_B-J)/J$ on the bubble volume.

B. Relative bubble velocity as a function of bubble volume

A liquid mass balance relative to a coordinate system fixed to the bubble gives

$$(U_{L,\mathrm{slug}}-U_B)A_{\mathrm{ch}}=(U_{L,\mathrm{film}}-U_B)A_{L,\mathrm{film}}. \tag{17}$$

Here, $U_{L,\mathrm{slug}}=J$ is the mean axial velocity of the liquid in the slug, A_{ch} is the cross-sectional area of the channel, and $U_{L,\mathrm{film}}$ is the mean axial liquid velocity in the liquid film with cross-sectional area $A_{L,\mathrm{film}}$. From Eq. (17) we obtain

$$Z \equiv \frac{U_B - J}{J} = \frac{U_B - U_{L,\mathrm{film}}}{J}\frac{A_{L,\mathrm{film}}}{A_{\mathrm{ch}}}. \tag{18}$$

While both $U_{L,\mathrm{film}}=U_{L,\mathrm{film}}(y)$ and $A_{L,\mathrm{film}}=A_{L,\mathrm{film}}(y)$ depend on the axial position y where the mass balance is taken, the above equation is nevertheless valid for any axial position where the bubble is present. It is, however, meaningful to consider that axial cross section where the bubble is largest and $A_{L,\mathrm{film}}$ is smallest. In all the present simulations, the bubble is axisymmetric and its largest diameter is D_B. For our square channel we then have $A_{\mathrm{ch}}=D_h^2$ and $A_{L,\mathrm{film}}^{\min}=D_h^2 - \pi D_B^2/4$. From Eq. (17), it follows for the mean velocity in the liquid film,

$$U_{L,\mathrm{film}}^{\max} = U_B - (U_B - J)\left(1 - \frac{\pi}{4}\frac{D_B^2}{D_h^2}\right)^{-1}. \tag{19}$$

Goldsmith and Mason[29] showed that for a long bubble in a circular capillary $U_{L,\mathrm{film}}/U_B$ strongly depends on the viscosity ratio μ_G/μ_L, while for an inviscid bubble the liquid surrounding the bubble in the region of constant film thickness is at rest. Here, we have $\mu_G/\mu_L=6.2\times10^{-4}$ and the evaluation of Eq. (19) for case A1 with terminal bubble diameter $D_B/D_h=0.809$ gives $U_{L,\mathrm{film}}^{\max}/U_B=0.075$, while for case B1 we have $D_B/D_h=0.843$ which yields $U_{L,\mathrm{film}}^{\max}/U_B=0.0045$. Since $U_{L,\mathrm{film}}^{\max} \ll U_B$ we may neglect $U_{L,\mathrm{film}}$ in Eq. (18) and obtain

$$Z \approx \frac{U_B}{J}\left(1 - \frac{\pi}{4}\frac{D_B^2}{D_h^2}\right). \tag{20}$$

Since D_B is a function of the capillary number[1] and Ca is proportional to U_B, the above equation is nonlinear. Furthermore, for the same value of Ca the bubble diameter may depend on the bubble volume, so that $D_B/D_h = f(\mathrm{Ca}, D_{\mathrm{eq}}/D_h)$. The results of Ho and Leal[15] for the flow of neutrally buoyant drops through a circular capillary show that for a given total superficial velocity J the drop diameter D_B increases with increasing drop volume and becomes constant if the ratio D_{eq}/D_h exceeds about 1. As the drop diameter increases, the drop occupies regions with lower velocity. Therefore, Ho and Leal[15] found that the ratio of drop velocity to total superficial velocity decreases with increasing drop volume but becomes independent of the drop volume as D_{eq}/D_h is increased above 0.9. Goldsmith and Mason[29] also observed these features in their investigation of the motion of very large bubbles. For the simulations displayed in Fig. 7, the values of J differ. However, we expect that for cases a–c where $D_{\mathrm{eq}}/D_h<1$ the bubble diameter D_B is mainly a function of D_{eq} and increases as D_{eq}/D_h increases. From Eq. (20) we see, therefore, that Z will decrease as D_{eq}/D_h increases from case a to c. This is the falling branch in Fig. 7. For cases f–h the ratio D_{eq}/D_h is larger than 1, so that D_B should only weakly increase as D_{eq} increases. On the other hand, D_B depends on Ca. For sufficiently long bubbles the bubble diameter decreases as the capillary number increases.[1] Both effects counteract and seem to be in balance for cases f–h since D_B/D_h is almost constant with a value of 0.849 (see Table II in Wörner *et al.*[36]). Therefore, according to Eq. (20) Z will mainly depend on the ratio U_B/J, which is increasing for cases d–h. This gives the rising branch in Fig. 7.

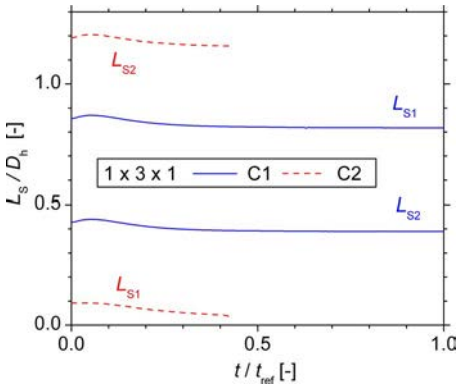

FIG. 8. (Color online) Time history of the slug lengths L_{S1} and L_{S2} for cases C1 and C2.

C. Stability for flow of small bubbles in large domain

From the previous discussions, the question arises if the stability of the bubble train flow for case B and its instability for case A originate mainly from the different bubble sizes or different liquid slug lengths. To investigate this topic we perform two additional simulations, where we use the large computational domain (nondimensional size of $1\times3\times1$). On the channel centerline we now place two bubbles of the smaller volume ($D_{\mathrm{eq}}/D_h=0.858$), which results in a gas holdup of 22%. For case C1 the ratio of the initial length of both slugs is $\lambda=0.5$, while for case C2 it is $\lambda=0.077$. The time history of the length of both slugs for cases C1 and C2 presented in Fig. 8 shows that case C2 is unstable and leads to coagulation while for case C1 both slug lengths seem to be constant in time. However, a close inspection of the data shows that the length of the longer slug is decreasing very slowly while that of the shorter slug is increasing very slowly. Therefore, we conclude that case C1 is stable. The velocity of both bubbles differ by a very small amount (about 0.04%) so it will take very long time until the lengths of both liquid slugs are equal. Since case C1 is stable while case C2 is unstable, we conclude that the stability is mainly determined by the length of the liquid slug and not by the bubble size. Therefore, we investigate next the difference in the structure of the liquid slugs for cases where the bubble train flow is stable and where it is unstable.

D. Flow structure in the liquid slug

To investigate the structure in the liquid slug we analyze the velocity field in a frame of reference moving with the mean axial velocity of the gas phase within the computational domain U_G. Since both bubbles have the same volume but move with slightly different velocity, U_G is equal to the arithmetic mean value of the translational velocities of the two bubbles. Figure 9 shows a visualization of the simulation results for cases A4 and A0g in such a frame of reference. In the right half of Figs. 9(a) and 9(b), the velocity field in the bubble and the liquid is displayed for the vertical midplane $z/L_{\mathrm{ref}}=0.5$. In the left half of the figure, the bubble shape is displayed together with trajectories of virtual particles that are released at certain positions within the liquid slug in this midplane. These trajectories are obtained by the module

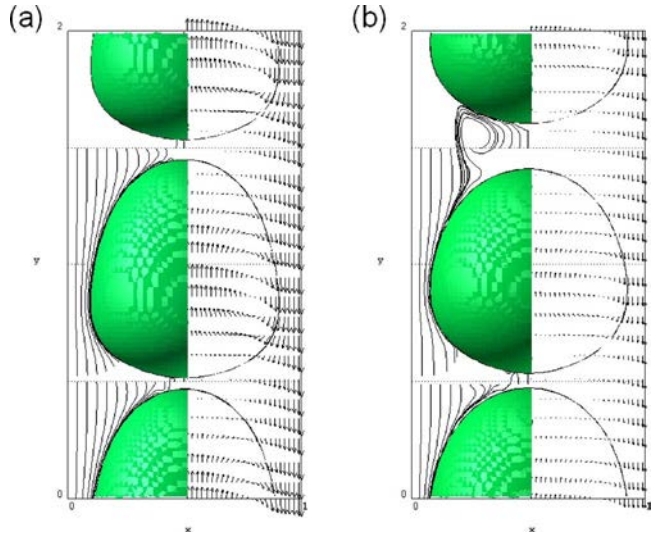

FIG. 9. (Color online) Visualization of particle trajectories (left half) and velocity vectors (right half) in moving frame of reference for plane $z/L_{\mathrm{ref}}=0.5$ for (a) case A4 for $t/t_{\mathrm{ref}}=1.235$ and (b) case A0g for $t/t_{\mathrm{ref}}=2.365$.

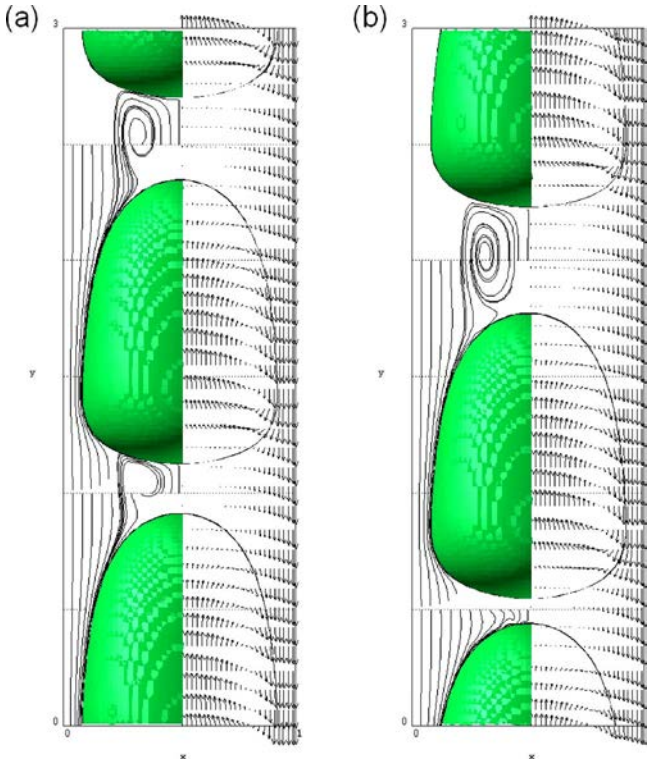

FIG. 10. (Color online) Visualization of particle trajectories (left half) and velocity vectors (right half) in moving frame of reference for plane $z/L_{\mathrm{ref}}=0.5$ for (a) case B3 for $t/t_{\mathrm{ref}}=2.575$ and (b) case B4 for $t/t_{\mathrm{ref}}=1.67$.

"streamlines" of the visualization software AVS/EXPRESS. Since the velocity field is not steady as long as the bubbles move with different velocities and the length of both liquid slugs is changing in time, these trajectories are not real streamlines but are, nevertheless, useful to illustrate the structure in the liquid slug. In Fig. 9, these virtual particles are injected at positions $y/L_{\mathrm{ref}}=0.5$ and 1.5 for different values of x. For case A4, Fig. 9(a) shows a typical bypass flow, i.e., all virtual particles with exceptions of those very close to the centerline of the channel move downstream and there is no recirculation in the liquid slug. The same hold for cases A1–A3. Only for case A0g the situation is different. As shown in Fig. 9(b), there exists a recirculation in the longer liquid slug.

In Fig. 10 we show similar visualizations for cases B3 and B4. For case B3 we observe a recirculation in both liquid slugs, whereas for case B4 the recirculation exists only in the longer liquid slug. It is interesting to note that for case B4 all virtual particle trajectories in the short liquid slug (without recirculation) move downstream. This is in contrast to the short slugs without recirculation displayed in Fig. 9 for cases A4 and A0g, where close to the centerline an upstream movement in this frame of reference can be observed. Figure 11 shows similar visualizations but for cases C1 and C2. For case C1 there is a recirculation in both liquid slugs, whereas for case C2 it exists only in the longer one. In the shorter slug of case C2, there exists an upward motion in a very small region close the centerline, similar to cases A4 and A0g. Note that the scale of the velocity vectors in Figs. 9–11 is the same, while in y-direction only every fourth vector is displayed.

Taylor[45] argued (for a detailed derivation, see Cox[47]) that for the streamline ahead of one long bubble that translates through a circular tube of radius R and leaves behind a stagnant liquid film of uniform thickness ηR, there are three possible patterns in a frame fixed to the bubble. These patterns depend on the fraction of liquid m left on the wall, which is given by $m=1-\eta^2=(U_B-U_{L,\mathrm{mean}})/U_B$. Here, $U_{L,\mathrm{mean}}$ is the mean velocity in the liquid ahead of the bubble. For $m>0.5$ there is one stagnation point on the nose of the bubble and no liquid recirculation in front of the bubble. For $m<0.5$ two streamline patterns are possible, namely, (i) one stagnation point on the nose of the bubble and a stagnation ring on the meniscus and (ii) two stagnation points on the axis. For both latter cases, there exists a recirculation in the liquid ahead of the bubble. Cox[47] experimentally confirmed the streamline pattern for $m>0.5$ and the stagnation ring pattern for $m<0.5$, while the pattern with two stagnation points on the axis for $m<0.5$ has never been found experimentally, but in numerical simulations.[40,48]

While the above results of Taylor and Cox are derived for a single long bubble that displaces a liquid in a tube and leaves behind a stagnant liquid film, it is clear that the analysis is of relevance for bubble train flow in noncircular ducts with nonstagnant liquid films as well. The critical issue for the streamline pattern arises from a comparison of the bubble velocity U_B with the centerline velocity of the fully developed laminar liquid flow ahead of the bubble, U_{cl}. A recirculation pattern in the liquid can occur for $U_B<U_{\mathrm{cl}}$ and thus for $(U_B-U_{L,\mathrm{mean}})/U_{L;\mathrm{mean}}<U_{\mathrm{cl}}/U_{L,\mathrm{mean}}-1$. For a laminar pipe flow it is $U_{\mathrm{cl}}/U_{L,\mathrm{mean}}=2$ and for the laminar flow in a square channel $U_{\mathrm{cl}}/U_{L,\mathrm{mean}}=2.0962$ (Shah and London[49]). For bubble train flow, the mean velocity within the liquid slug is $U_{L,\mathrm{mean}}=J$, which yields $Z<U_{\mathrm{cl}}/U_{L,\mathrm{mean}}-1$. Therefore, a recirculation may occur in a tube for $Z<1$ and in a square duct for $Z<1.0962$. In terms of $W\equiv(U_B-J)/U_B=ZJ/U_B$ the latter relations are not easy to evaluate since

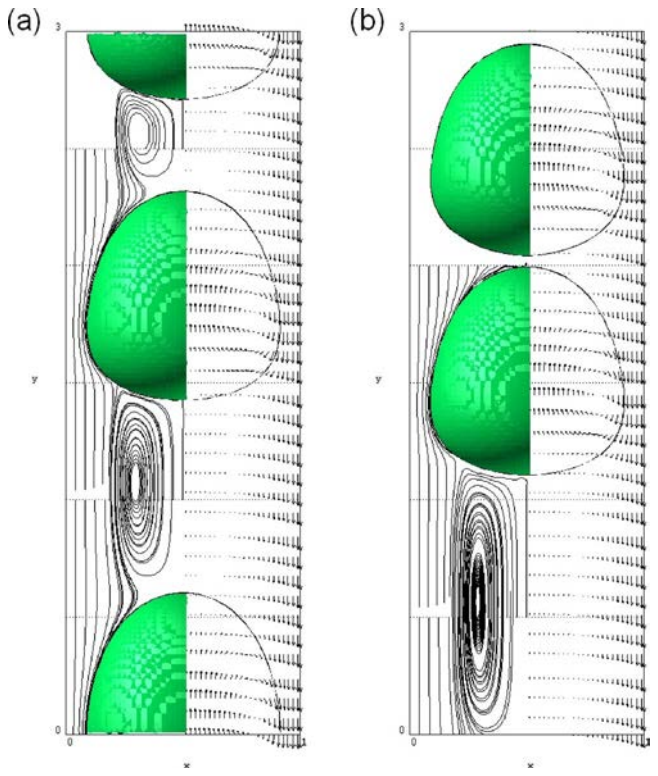

FIG. 11. (Color online) Visualization of particle trajectories (left half) and velocity vectors (right half) in moving frame of reference for plane $z/L_{\mathrm{ref}}=0.5$ for (a) case C1 for $t/t_{\mathrm{ref}}=0.955$ and (b) case C2 for $t/t_{\mathrm{ref}}=0.37$.

there additionally the ratio J/U_B is of relevance, which depends on the capillary number.[1] In the present simulations, Z is always less than about 0.8 and W always less than 0.45, so one can expect a recirculation in the liquid slug to occur, supposed the slug is sufficiently long.

Thulasidas *et al.*[50] investigated experimentally the flow pattern in liquid slugs in cocurrent upward bubble train flow both in circular and square capillaries with $D_h=2$ mm. Depending on the value of the capillary number, recirculation vortices inside the liquid slug were observed in the square channel for $\mathrm{Ca}=0.37$, while a complete bypass flow was found for $\mathrm{Ca}=0.54$. The transition occurs for $\mathrm{Ca}\geq 0.47$. Thulasidas *et al.*[50] also pointed out the role of the length of the liquid slug for the velocity profile. The velocity profiles were found to be Poiseuille-flow profiles at a region between adjacent bubbles, except for very short liquid slugs. For liquid slugs longer than $L_s/D_h=1.5$ the Poiseuille profile is fully developed and the streamlines are straight in the central region of the liquid slug. For shorter liquid slugs, the velocity field is not fully developed and streamlines are curved everywhere. In the present simulations, it is $\mathrm{Ca}\approx 0.21$ for cases A1–A3, $\mathrm{Ca}\approx 0.11$ for case A0g, $\mathrm{Ca}\approx 0.23$ for cases B1–B4, and $\mathrm{Ca}\approx 0.16$ for cases C1–C2. Thus, for all cases Ca is less than 0.37 and the recirculation streamline patterns in long liquid slugs displayed in Figs. 9–11 are in agreement with experimental results.[50] Tsoligkas *et al.*[51] repeated the experiments of Thulasidas *et al.*[1,50] for cocurrent downward flow in a square channel. They investigated the liquid velocity profiles in the center of the liquid slug and found that short liquid slugs with $L_s<D_h$ exhibited a flat axial velocity profile while long slugs ($L_s>D_h$) obey a parabolic one and thus show a recirculation pattern. Kashid *et al.*[52] showed in their experiments that a recirculation in the liquid slug even exists in a capillary channel having dimensions of only $70\times 12\ \mu\mathrm{m}^2$.

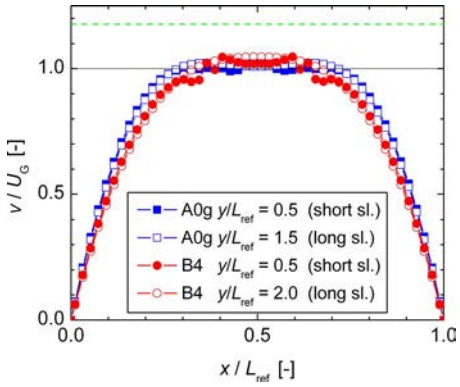

FIG. 12. (Color online) Profiles of normalized vertical velocity v/U_G in the middle of the two liquid slugs. The instants in time for cases A0g and B4 correspond to those in Figs. 9(b) and 10(b). The position in z-direction is $z/L_{\mathrm{ref}}=0.49$ (due to the staggered grid). The dashed horizontal line corresponds to the maximum velocity of a fully developed Poiseuille profile.

A comparison of all presents simulations regarding the structure of the liquid slugs suggests that there is a minimum length of the liquid slug required so that a recirculation can exist. For all simulations where the ratio L_s/D_h is less then about 0.1 there is no recirculation but bypass flow. Instead, for all cases where L_s/D_h is larger than about 0.2 we find a recirculation in the liquid slug. Therefore, the minimum slug length above which a recirculation in the liquid slug can occur is in the range of $0.1<L_s/D_h<0.2$. This estimation is consistent with the numerical computations of Fujioka and Grotberg[53] who report for a 2D channel with $L_s/D_h=0.25$ a recirculation pattern in the liquid slug. According to Thulasidas *et al.*,[50] such short liquid slugs should not have a fully developed Poiseuille profile. The standard formula for the estimation of the entrance length L_e in laminar flow is $L_e/D_h=0.06\,\mathrm{Re}_{D_h}$. With J as the mean velocity in the liquid slug, the corresponding Reynolds number is about 2.3 for the runs of case B. This yields $L_e/D_h\approx 0.14$, a value that remarkably lies in the middle of the range of $0.1<L_s/D_h<0.2$. This result suggests that the above laminar entrance length formula may serve as a first guess to estimate the critical length of a liquid slug, above which a recirculation pattern may occur. However, this aspect needs further investigations.

From the present results it appears that the occurrence of a recirculation pattern in the liquid slug favors the stability of bubble train flow. Namely, all cases where there is bypass flow in both liquid slugs are unstable (cases A1–A4) while all cases where there is a recirculation in both liquid slugs are stable (cases B1, B2, B3, and C1). For situations where there is recirculation only in one liquid slug, the situation is more subtle. For cases A0g and C2 the bubble train flow is unstable, while for case B4 it is stable. To investigate the reason for this, we analyze profiles of the axial velocity within the liquid slug. In Fig. 12 we show such profiles

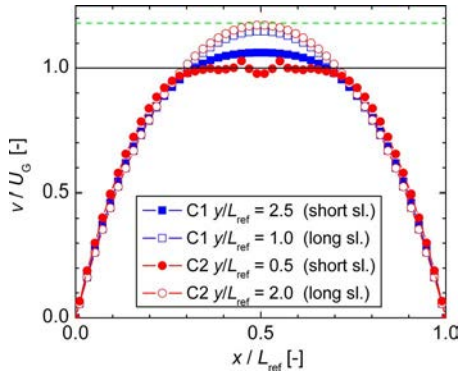

FIG. 13. (Color online) Profiles of normalized vertical velocity v/U_G in the middle of the two liquid slugs. The instants in time for cases C1 and C2 correspond to those in Figs. 11(a) and 11(b). The position in z-direction is $z/L_{\mathrm{ref}}=0.49$. The dashed horizontal line corresponds to the maximum velocity of a fully developed Poiseuille profile.

within the middle of the two liquid slugs for cases A0g and B4. We see that the profiles are not parabolic but rather flat. The normalized maximum velocity for a fully developed Poiseuille profile is given by $U_{\mathrm{cl}}=2.0962J$. For case B4 the ratio $U_{\mathrm{cl}}/U_G=2.0962J/U_G$ takes a value of 1.177 and is shown in Fig. 12 as dashed horizontal line. The flat profiles indicate that the liquid slugs are too short for a Poiseuille profile to develop. The profiles for the shorter slugs of cases A0g and B4 show a symmetrical but unusual behavior in the middle of the channel, indicating that vortical structures of low amplitude may exist in a small region within the slug close to the centerline of the channel. Obviously, these vortical structures are different for cases A0g and B4. An important difference between the velocity profiles for cases A0g and B4 in Fig. 12 concerns the magnitude of velocity in both slugs on the centerline. For case A0g the centerline velocity in the short slug is higher than that in the long slug, whereas in case B4 it is vice versa. Accordingly, for case A0g the bubble behind the short slug is faster than the one behind the long slug and this leads to coagulation. On the other hand, for case B4 the bubble behind the short slug is slower than that behind the long slug, leading finally to liquid slugs of equal length and stable bubble train flow.

In Fig. 13 we show similar profiles, but for cases C1 and C2. The velocity profiles in the longer slug of both cases are almost parabolic, while the profiles in the short slug are much flatter. The normalized maximum velocity of a fully developed Poiseuille profile takes a value of $U_{\mathrm{cl}}/U_G=1.181$. For the longer liquid slug of case C2 with a length of $L_s/D_h\approx 1.2$ the maximum velocity is close to this value. This supports the experimental finding of Thulasidas *et al.*[50] that the Poiseuille profile within the liquid slug is fully developed for $L_s/D_h\geq 1.5$. In Fig. 13, the axial velocity of the liquid slug on the centerline is smaller for the shorter slug than for the longer one, both for cases C1 and C2. However, case C1 is stable while case C2 leads to coagulation. This indicates that a critical length of the liquid slug may exist, which must be exceeded so that a stable bubble train flow can develop. For case C2, the initial length of the shorter slug was only $L_s^0/D_h=0.092$. Obviously, this value was below this critical length while for case C1 the value of $L_s^0/D_h=0.428$ was sufficiently large.

Pinto *et al.*[20] argued (see also the discussion in Sec. I) that for a laminar flow in the liquid slug, the velocity profile in the liquid emerging from the wake of the leading bubble is decisive for the velocity of the trailing bubble to be smaller or larger than that of the leading bubble. The authors state that for the case where the velocity profile in the liquid slug in the circular pipe is uniform or almost uniform and is lower than $2U_{L,\mathrm{mean}}$ (the maximum liquid velocity in a pipe when the velocity profile is parabolic) coalescence does not occur. On the other hand, when the profile has a region where the velocity is greater than $2U_{L,\mathrm{mean}}$, this results in coalescence. In the present simulations, we have always the first case, i.e., $U_{\mathrm{cl}}<2.0962J$ which means that according to Pinto *et al.*[20] no coagulation should occur. However, the present results indicate that there can be coagulation or not, depending on different aspects, mainly on the length of the liquid slug and its local flow structure. One may expect that in short liquid slugs the local flow structure may depend on the interface curvature of both, the rear of the leading and the front of the trailing bubble. The present results give strong indication that a simple criterion like that of Campana *et al.*,[31] who found that for a given value of Ca the stability of bubble train flow depends only on Re, is not realistic for many cases. This is supported by a follow up study of the authors,[32] which shows the existence of a small stable region whose size increases as the Laplace number is augmented. In both latter studies the flow in the bubble is neglected and the liquid film thickness is assumed to be uniform. These assumptions are also made by Fujioka and Grotberg[53] who nevertheless report for finite Reynolds number a significant interaction between the leading and the trailing menisci and their local flow effects, when the liquid slug length decreases below the channel width. In the present simulations we have a finite viscosity ratio μ_G/μ_L and there is—due to the continuity of the tangential shear stress at the interface—a strong coupling between the flow inside the bubble and both, the flow in the liquid film[29] and the flow in the wake of the bubble.[34] From the analysis of the present velocity profiles in short liquid slugs, it appears that for the stability of bubble train flow the complex interaction between the wake of the leading bubble and the flow field in front of the trailing bubble is a critical issue which is yet not fully understood.

V. CONCLUSIONS

In this work, a computational study is carried out to evaluate the stability of a train of gas bubbles of equal size that translate within a continuous wetting liquid phase through a straight square vertical minichannel. The computational setup consists of an axially periodic domain with two bubbles placed on the centerline of the channel, resulting in two liquid slugs of variable length, depending on the initial bubble-to-bubble distance. For cases where the initial length of the two liquid slugs is identical, the bubble train flow is always stable. When the initial lengths of the two liquid slugs differ, a relative velocity between bubbles occurs and

the bubble train flow may be stable (the two liquid slug lengths become finally equal) or unstable (one liquid slug disappears and coagulation occurs). Our results show that the stability of bubble train flow is related to the flow structure in the liquid slug. In sufficiently long liquid slugs (with a length larger than about one-fifth of the channel width), a recirculation pattern exists, while for shorter liquid slugs a bypass flow occurs. The bubble train flow is found to be stable if a recirculation pattern exists in both liquid slugs, while it is unstable if bypass flow occurs in both liquid slugs. Therefore, in bubble train flow, a recirculation in the liquid slugs prevents bubble coagulation and coalescence. If there is a recirculation in one liquid slug and bypass flow in the other, then the bubble train flow may be stable or not, depending on the local flow field in the liquid slugs close to the channel centerline. In conclusion, the present results strongly suggest that a simple criterion, which relates the stability of bubble train flow to critical values of the capillary and Reynolds number only, is not valid, in general. Instead, the length of the liquid slugs is also important and must be taken into account.

From the present study, several suggestions for future work arise. One key to understand the stability of bubble train flow is the dependence of the nondimensional relative velocity $(U_B - J)/J$ on the liquid slug length for a given bubble size and driving pressure gradient (without buoyancy). In a future computational study, we will determine this relation for different values of the length of the unit cell. Further interesting topics are (i) the influence of gravity/buoyancy (i.e., the stability of cocurrent downward flow), (ii) the critical length of a liquid slug for which the transition from bypass to recirculation flow occurs for a given capillary number, (iii) the stability of the train flow of long bubbles at high values of the capillary number where only bypass flow can exist, and (iv) the critical distance for which interactions of short bubbles diminish. Of course, the ultimate aim—to identify criteria for the stability of bubble train flow—must also be guided and confirmed by experimental studies.

ACKNOWLEDGMENTS

The supports of the Institute of Science and Technology at Sakarya University, Forschungszentrum Karlsruhe and EU LLP program are gratefully acknowledged.

APPENDIX: NUMERICAL METHOD

In this appendix we give some details about the numerical method. We first describe our exact plane interface reconstruction algorithm[33] (EPIRA). It can be used for a structured orthogonal nonequidistant fixed grid. EPIRA reconstructs a plane 3D-interface exactly, regardless of its orientation. We consider a functional interface of zero thickness, which can be locally described by a single valued height function $\xi = h(\zeta, \eta)$, where (ζ, η, ξ) define a local Cartesian coordinate system. Expanding $h(\zeta, \eta)$ in a Taylor series around the point (ζ_0, η_0) and considering only the linear terms yields

$$h(\zeta, \eta) \cong h_0 + \alpha(\zeta - \zeta_0) + \beta(\eta - \eta_0). \tag{A1}$$

To reconstruct the interface orientation and position, we need to determine a unit normal vector to the interface and a point lying on the interface. We illustrate the procedure for a rectangular mesh cell (i,j,k) with a liquid volumetric fraction $0 < f_{i,j,k} < 1$. We denote the six faces of this mesh cell by E (east), located at $x_{i+1/2}$, W (west) at $x_{i-1/2}$, N (north) at $z_{k+1/2}$, S (south) at $z_{k-1/2}$, F (front) at $y_{j-1/2}$, and B (back) at $y_{j+1/2}$. For each face we determine if it is cut by the gas/liquid (g/l) interface, e.g., face E (east) is a g/l-interface face if $0 < f_{i+1,j,k} < 1$. Next, we determine for each g/l-interface face a tangential vector to the interface. This is illustrated for face E in Fig. 14(a), where we assume that the local coordinate system (ζ, η, ξ) coincides with the global coordinate system (x,y,z). If the plane $h(x,y)$ does not cut the upper or lower faces of the cells (i,j,k) and $(i+1,j,k)$, then $N_{i,j,k}$, $S_{i,j,k}$, $N_{i+1,j,k}$, and $S_{i+1,j,k}$ are not g/l-interface faces and it is

$$f_{i,j,k} = \frac{1}{\Delta x_i \Delta y_j \Delta z_k} \int_0^{\Delta x_i} \int_0^{\Delta y_j} h(x,y)\,dy\,dx,$$
$$f_{i+1,j,k} = \frac{1}{\Delta x_{i+1} \Delta y_j \Delta z_k} \int_{\Delta x_i}^{\Delta x_i + \Delta x_{i+1}} \int_0^{\Delta y_j} h(x,y)\,dy\,dx. \tag{A2}$$

By inserting Eq. (A1) in Eq. (A2), performing the integrations, and subtracting $f_{i,j,k}$ from $f_{i+1,j,k}$, we obtain for the interface slope α_E and the unit tangential vector $\hat{\mathbf{t}}_E$ at face E the results

$$\alpha_E = \alpha_{i+1/2,j,k} = \frac{2\Delta z_k}{\Delta x_i + \Delta x_{i+1}} (f_{i+1,j,k} - f_{i,j,k}), \tag{A3}$$

$$\hat{\mathbf{t}}_E = \frac{1}{\sqrt{1 + \alpha_E^2}} \begin{pmatrix} 1 \\ 0 \\ \alpha_E \end{pmatrix}. \tag{A4}$$

This tangential vector is exact supposed the lower and upper integration limits in Eq. (A2) are correct, which requires that $N_{i,j,k}$, $S_{i,j,k}$, $N_{i+1,j,k}$, and $S_{i+1,j,k}$ are not g/l-interface faces. Otherwise, e.g., for the situation displayed in Fig. 14(b), the integration limits must be adjusted to account for the intersections of the g/l-interface with the lower/upper cell faces, respectively. This requires the consideration of several distinct situations which we want to avoid. For this purpose, we extend the integration domain and consider a pair of double cells $(i,j,k)+(i,j,k+1)$ and $(i+1,j,k)+(i+1,j,k+1)$, see Fig. 14(c). For each double cell, Eq. (A4) yields the exact value for $\hat{\mathbf{t}}_E$ by replacing in Eq. (A3) Δz_k by $(\Delta z_k + \Delta z_{k+1})$, $f_{i,j,k}$ by $(f_{i,j,k}\Delta z_k + f_{i,j,k+1}\Delta z_{k+1})/(\Delta z_k + \Delta z_{k+1})$ and $f_{i+1,j,k}$ by $(f_{i+1,j,k}\Delta z_k + f_{i+1,j,k+1}\Delta z_{k+1})/(\Delta z_k + \Delta z_{k+1})$, respectively. A similar procedure is used when $S_{i,j,k}$ or $S_{i+1,j,k}$ are g/l-interface faces.

When $N_{i,j,k+1}$, $N_{i+1,j,k+1}$, $S_{i,j,k-1}$, or $S_{i+1,j,k-1}$ are g/l-interface faces, one upper and/or lower extension is insufficient to obtain α_E exactly. Since we do not want to lose the locality of the reconstruction, we perform at most one extension above and/or one below the basic pair of cells. If this is not sufficient to determine α_E exactly, then we set the slope

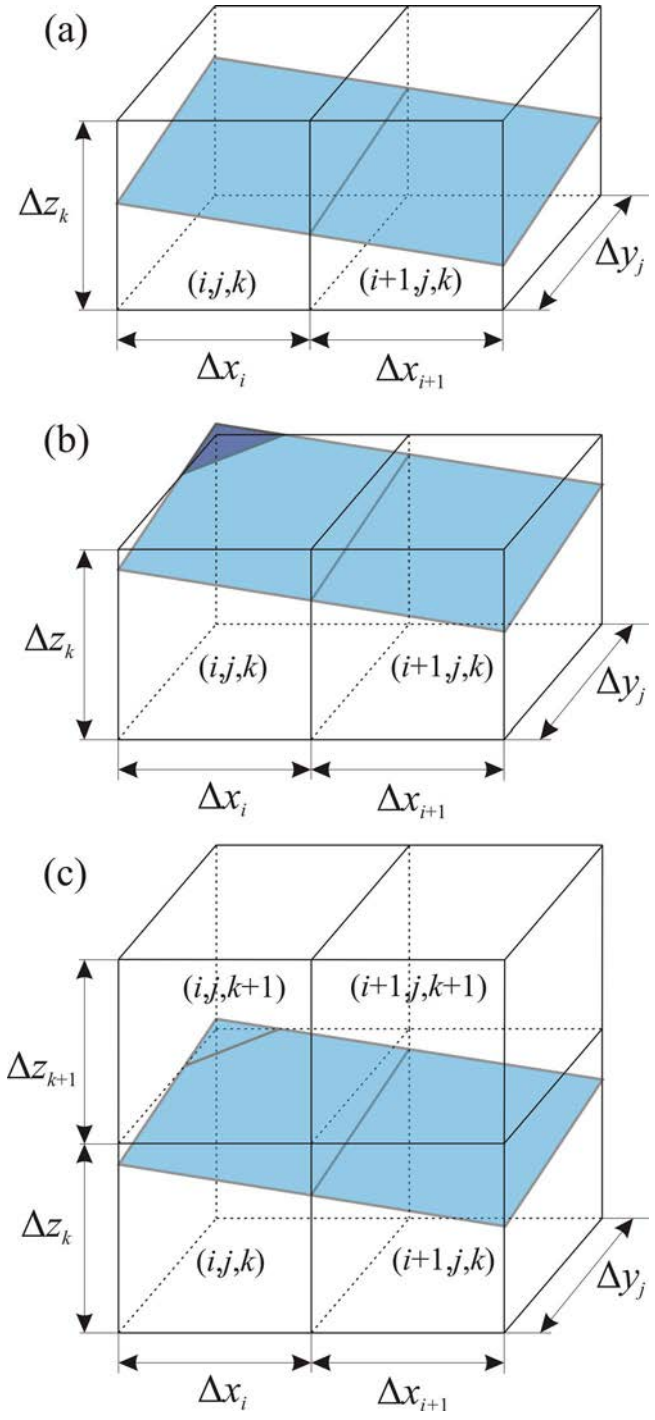

FIG. 14. (Color online) (a) A pair of mesh cells (i,j,k) and $(i+1,j,k)$ with a plane representing the interface, the liquid being below the plane. (b) Situation where face $N_{i,j,k}$ is a g/l-interface face. (c) Extension of the left and right integration domain to obtain α_E and $\hat{\mathbf{t}}_E$ for this case exactly.

β in Eq. (A1) to zero and thereby simplify the 3D problem to a 2D one. An approximation for the slope α_E is then determined from the 2D FLAIR algorithm of Ashgriz and Poo,[54] which we extended for nonequidistant grids. The unit tangential vector is flagged as *exact*, if the slope is determined via Eq. (A3) (with or without extension), and is flagged as *inexact* if it is computed from the 2D FLAIR algorithm. For computational reasons, we set the tangential vector to the null vector when a face is not a g/l-interface face and flag it as inexact. Next, we determine for each coordinate direction a representative tangential vector as follows. If $\hat{\mathbf{t}}_E$ and $\hat{\mathbf{t}}_W$ are marked with the same flag (i.e., both exact or inexact), then $\hat{\mathbf{t}}_{EW}$ is obtained by averaging $\hat{\mathbf{t}}_{EW}=(\hat{\mathbf{t}}_E+\hat{\mathbf{t}}_W)/|\hat{\mathbf{t}}_E+\hat{\mathbf{t}}_W|$. Otherwise, either $\hat{\mathbf{t}}_E$ or $\hat{\mathbf{t}}_W$ is selected as representative, depending which one is the exact one. We flag $\hat{\mathbf{t}}_{EW}$ as exact if $\hat{\mathbf{t}}_E$ or $\hat{\mathbf{t}}_W$ or both are exact and as inexact otherwise. The representative unit tangential vectors for the other coordinate directions, $\hat{\mathbf{t}}_{NS}$ and $\hat{\mathbf{t}}_{FB}$, are determined similarly. Using these three representative unit tangential vectors, a minimum of one and maximum of three preliminary unit normal vectors are computed,

$$\hat{\mathbf{n}}_1=\frac{\hat{\mathbf{t}}_{EW}\times\hat{\mathbf{t}}_{NS}}{|\hat{\mathbf{t}}_{EW}\times\hat{\mathbf{t}}_{NS}|},\quad \hat{\mathbf{n}}_2=\frac{\hat{\mathbf{t}}_{NS}\times\hat{\mathbf{t}}_{FB}}{|\hat{\mathbf{t}}_{NS}\times\hat{\mathbf{t}}_{FB}|},\quad \hat{\mathbf{n}}_3=\frac{\hat{\mathbf{t}}_{FB}\times\hat{\mathbf{t}}_{EW}}{|\hat{\mathbf{t}}_{FB}\times\hat{\mathbf{t}}_{EW}|}. \tag{A5}$$

If necessary, each preliminary normal vector is reorientated to point inside the liquid. By averaging the preliminary normal vectors, and by taking into account if the representative tangential unit vectors are exact or not, we obtain eventually the representative cell-centered unit normal vector $\hat{\mathbf{n}}_{i,j,k}$. For the situation illustrated in Fig. 13(a), the vector $\hat{\mathbf{t}}_{NS}$ is zero, which implies that only the normal vector $\hat{\mathbf{n}}_3$ exists, so no averaging is required. Finally, the interface reconstruction is completed by determining a point lying in the plane. This is done iteratively by shifting the plane until the correct liquid volumetric fraction $f_{i,j,k}$ of this mesh cell is recovered.

For time advancement of the f-equation, Eq. (2), from time step n to $n+1$, we compute the fluxes of the liquid phase across the mesh cell faces by a "naive unsplit" method. Thus, the liquid fluxes in the three coordinate directions are computed simultaneously, and only one reconstruction step per time step is performed. For each face of an interfacial mesh cell, a flux volume in form of a cuboid is computed. The base of the cuboid is the cell-face area and its depth is the face-centered (staggered) velocity at time step n multiplied by the time step width Δt. Based on the reconstructed interface, the volume of the liquid phase within the cuboid is computed and is fluxed to the neighboring mesh cell which shares the same face. When the flow is oblique to the cell faces, cuboids resulting from different cell faces may overlap, and liquid volume may be advected more than once. In such a case it happens that, after the advection step, there may remain interface-cells with a very small fraction of liquid, $0<f_{i,j,k}<\varepsilon$, or gas, $1-\varepsilon<f_{i,j,k}<1$, and only two g/l-interface faces. Such a configuration is not meaningful for EPIRA, so we redistribute the liquid or gas to neighboring interface mesh cells. The value of ε is related to the residuum of the divergence of the velocity field and the time step width. In our simulations we set $\varepsilon=10^{-6}$.

We now describe the numerical method for solution of the momentum equation, Eq. (3). The solution strategy is based on a projection method. The predictor step includes all terms but the pressure term

$$\frac{\partial(\tilde{\rho_m}\tilde{\mathbf{v}_m})}{\partial\theta} = -\nabla\cdot\rho_m\mathbf{v}_m\mathbf{v}_m + \frac{1}{\mathrm{Re}_{\mathrm{ref}}}\nabla\cdot\mu_m(\nabla\mathbf{v}_m + (\nabla\mathbf{v}_m)^T) + \frac{a_i^*\kappa^*\hat{\mathbf{n}}_i}{\mathrm{We}_{\mathrm{ref}}} - (1-f)\frac{\mathrm{Eo}_{\mathrm{ref}}}{\mathrm{We}_{\mathrm{ref}}}\hat{\mathbf{e}}_g + \mathrm{Fr}_{\mathrm{ref}}\hat{\mathbf{e}}_g + \frac{\mathrm{Eu}_{\mathrm{ref}}}{L^*_{\mathrm{axial}}}\hat{\mathbf{e}}_{\mathrm{axial}} = \mathcal{L}. \tag{A6}$$

It is performed by an explicit third order Runge–Kutta scheme,

$$\begin{aligned}
\rho_m^{(1)}\mathbf{v}_m^{(1)} &= \rho_m^n\mathbf{v}_m^n + \Delta t\mathcal{L}(\rho_m^n,\mu_m^n,\mathbf{v}_m^n,f^n),\\
\rho_m^{(2)}\mathbf{v}_m^{(2)} &= \tfrac{3}{4}\rho_m^n\mathbf{v}_m^n + \tfrac{1}{4}\rho_m^{(1)}\mathbf{v}_m^{(1)} + \tfrac{1}{4}\Delta t\mathcal{L}(\rho_m^{(1)},\mu_m^{(1)},\mathbf{v}_m^{(1)},f^{(1)}),\\
\tilde{\rho_m}\tilde{\mathbf{v}_m} &= \tfrac{1}{3}\rho_m^n\mathbf{v}_m^n + \tfrac{2}{3}\rho_m^{(2)}\mathbf{v}_m^{(2)} + \tfrac{2}{3}\Delta t\mathcal{L}(\rho_m^{(2)},\mu_m^{(2)},\mathbf{v}_m^{(2)},f^{(2)}),
\end{aligned} \tag{A7}$$

where the intermediate time levels are set as

$$\begin{aligned}
f^{(1)} &= f^{(2)} = f^{n+1},\\
\rho_m^{(1)} &= \rho_m^{(2)} = \tilde{\rho_m} = \rho_m^{n+1},\\
\mu_m^{(1)} &= \mu_m^{(2)} = \mu_m^{n+1}.
\end{aligned} \tag{A8}$$

Treating the pressure term implicitly, the corrector step is

$$\frac{\rho_m^{n+1}\mathbf{v}_m^{n+1} - \tilde{\rho_m}\tilde{\mathbf{v}_m}}{\Delta t} = -\nabla P^{n+1}. \tag{A9}$$

Applying the divergence operator to Eq. (A9) and introducing the continuity equation (1) yields the Poisson equation

$$\nabla\cdot\left(\frac{\Delta t}{\rho_m^{n+1}}\nabla P^{n+1}\right) = \nabla\cdot\tilde{\mathbf{v}_m}, \tag{A10}$$

which is solved by a conjugate gradient method.[55]

The spatial discretization of the above equations is based on a staggered grid, where second order central difference approximations are used for the convective and diffusive terms. Velocities at nonstaggered positions are obtained by linear interpolation. The mixture density and viscosity are, however, not interpolated but are determined as follows. Taking into account the actual interface location, e.g., in cell (i,j,k) and cell $(i+1,j,k)$, we compute the liquid volumes within the two half-cells $[x_{i,j,k},x_{i+1/2,j,k}]\times[y_{i,j-1/2,k},y_{i,j+1/2,k}]\times[z_{i,j,k-1/2},z_{i,j,k+1/2}]$ and $[x_{i+1/2,j,k},x_{i+1,j,k}]\times[y_{i,j-1/2,k},y_{i,j+1/2,k}]\times[z_{i,j,k-1/2},z_{i,j,k+1/2}]$, respectively. We then sum up the liquid volume in both half-cells and divide the result by the volume of both half-cells. This yields $f_{i+1/2,j,k}$ from which $\rho_{i+1/2,j,k}$ can be computed. The quantity $f_{i+1/2,j+1/2,k}$ needed for μ_m in the diffusive term is computed similarly, taking into account four quarter-cells. We finally illustrate the discretization of the surface tension term for the first component of the momentum equation, which is

$$S_{i+1/2,j,k} = \frac{1}{\mathrm{We}_{\mathrm{ref}}}a^*_{i;i+1/2,j,k}\kappa^*_{i+1/2,j,k}\hat{\mathbf{n}}_{i+1/2,j,k}. \tag{A11}$$

Since the EPIRA algorithm yields the interface unit normal vector at cell centers, we compute the staggered one from averaging

$$\hat{\mathbf{n}}_{i+1/2,j,k} = \frac{\hat{\mathbf{n}}_{i,j,k} + \hat{\mathbf{n}}_{i+1,j,k}}{|\hat{\mathbf{n}}_{i,j,k} + \hat{\mathbf{n}}_{i+1,j,k}|}. \tag{A12}$$

Note that in any mesh cell which is not an interface cell, we set $\hat{\mathbf{n}}_{i,j,k}$ to the null vector. The nondimensional interface curvature is computed from the gradient of the unit normal vector, $\kappa^* = -\nabla\cdot\hat{\mathbf{n}}$. For the first component of the momentum equation, it reads

$$\kappa^*_{i+1/2,j,k} = -\left(\frac{n_{x;i+1,j,k} - n_{x;i,j,k}}{\Delta x} + \frac{n_{y;i+1/2,j+1/2,k} - n_{y;i+1/2,j-1/2,k}}{\Delta y} + \frac{n_{z;i+1/2,j,k+1/2} - n_{z;i+1/2,j,k-1/2}}{\Delta z_k}\right). \tag{A13}$$

Again, the staggered values of the unit normal vector are obtained by averaging

$$\begin{aligned}
\hat{\mathbf{n}}_{i+1/2,j\pm1/2,k} &= \frac{\hat{\mathbf{n}}_{i,j,k} + \hat{\mathbf{n}}_{i,j\pm1,k} + \hat{\mathbf{n}}_{i+1,j,k} + \hat{\mathbf{n}}_{i+1,j\pm1,k}}{|\hat{\mathbf{n}}_{i,j,k} + \hat{\mathbf{n}}_{i,j\pm1,k} + \hat{\mathbf{n}}_{i+1,j,k} + \hat{\mathbf{n}}_{i+1,j\pm1,k}|},\\
\hat{\mathbf{n}}_{i+1/2,j,k\pm1/2} &= \frac{\hat{\mathbf{n}}_{i,j,k} + \hat{\mathbf{n}}_{i,j,k\pm1} + \hat{\mathbf{n}}_{i+1,j,k} + \hat{\mathbf{n}}_{i+1,j,k\pm1}}{|\hat{\mathbf{n}}_{i,j,k} + \hat{\mathbf{n}}_{i,j,k\pm1} + \hat{\mathbf{n}}_{i+1,j,k} + \hat{\mathbf{n}}_{i+1,j,k\pm1}|}.
\end{aligned} \tag{A14}$$

The nondimensional interfacial area concentration $a^*_{i;i+1/2,j,k}$ is computed by summing up the interfacial area in the two half-cells $[x_{i,j,k},x_{i+1/2,j,k}]\times[y_{i,j-1/2,k},y_{i,j+1/2,k}]\times[z_{i,j,k-1/2},z_{i,j,k+1/2}]$ and $[x_{i+1/2,j,k},x_{i+1,j,k}]\times[y_{i,j-1/2,k},y_{i,j+1/2,k}]\times[z_{i,j,k-1/2},z_{i,j,k+1/2}]$ and by dividing the result by the volume of both half-cells.

[1] T. C. Thulasidas, M. A. Abraham, and R. L. Cerro, "Bubble-train flow in capillaries of circular and square cross-section," Chem. Eng. Sci. **50**, 183 (1995).

[2] J. L. Williams, "Monolith structures, materials, properties and uses," Catal. Today **69**, 3 (2001).

[3] S. Roy, T. Bauer, M. Al-Dahhan, P. Lehner, and T. Turek, "Monoliths as multiphase reactors: A review," AIChE J. **50**, 2918 (2004).

[4] M. T. Kreutzer, F. Kapteijn, J. A. Moulijn, and J. J. Heiszwolf, "Multiphase monolith reactors: Chemical reaction engineering of segmented flow in microchannels," Chem. Eng. Sci. **60**, 5895 (2005).

[5] V. Haverkamp, V. Hessel, H. Löwe, G. Menges, M. J. F. Warnier, E. V. Rebrov, M. H. L. M. de Croon, J. C. Schouten, and M. Liauw, "Hydrodynamics and mixer-induced bubble formation in micro bubble columns with single and multiple-channels," Chem. Eng. Technol. **29**, 1015 (2006).

[6] A. Günther, M. Jhunjhunwala, M. Thalmann, M. A. Schmidt, and K. F. Jensen, "Micromixing of miscible liquids in segmented gas-liquid flow," Langmuir **21**, 1547 (2005).

[7] M. Muradoglu, A. Günther, and H. A. Stone, "A computational study of axial dispersion in segmented gas-liquid flow," Phys. Fluids **19**, 072109 (2007).

[8] M. Prakash and N. Gershenfeld, "Microfluidic bubble logic," Science **315**, 832 (2007).

[9] A. Günther and K. F. Jensen, "Multiphase microchemical systems: From flow characteristics to chemical and materials synthesis," Lab Chip **6**, 1487 (2006).

[10] P. Garstecki, M. J. Fuerstman, H. A. Stone, and G. M. Whitesides, "Formation of droplets and bubbles in a microfluidic T-junction–scaling and mechanism of break-up," Lab Chip **6**, 437 (2006).

[11]T. Kraus, A. Günther, N. Mas, M. A. Schmidt, and K. F. Jensen, "An integrated multiphase flow sensor for microchannels," Exp. Fluids **36**, 819 (2004).
[12]H. Song, J. D. Tice, and R. F. Ismagilov, "A microfluidic system for controlling reaction networks in time," Angew. Chem., Int. Ed. **42**, 768 (2003).
[13]B. Zheng and R. F. Ismagilov, "A microfluidic approach for screening submicroliter volumes against multiple reagents by using preformed arrays of nanoliter plugs in a three-phase liquid/liquid/gas flow," Angew. Chem., Int. Ed. **44**, 2520 (2005).
[14]D. L. Chen, L. Li, S. Reyes, D. N. Adamson, and R. F. Ismagilov, "Using three-phase flow of immiscible liquids to prevent coalescence of droplets in microfluidic channels: Criteria to identify the third liquid and validation with protein crystallization," Langmuir **23**, 2255 (2007).
[15]B. P. Ho and L. G. Leal, "The creeping motion of liquid drops through a circular tube of comparable diameter," J. Fluid Mech. **71**, 361 (1975).
[16]W. A. Hyman and R. Skalak, "Viscous flow of a suspension of liquid drops in a cylindrical tube," Appl. Sci. Res. **26**, 27 (1972).
[17]R. Moissis and P. Griffith, "Entrance effects in a two-phase slug flow," ASME J. Heat Transfer **84**, 29 (1962).
[18]C. A. Talvy, L. Shemer, and D. Barnea, "On the interaction between two consecutive elongated bubbles in a vertical pipe," Int. J. Multiphase Flow **26**, 1905 (2000).
[19]A. M. F. R. Pinto and J. B. L. M. Campos, "Coalescence of two gas slugs rising in a vertical column of liquid," Chem. Eng. Sci. **51**, 45 (1996).
[20]A. M. F. R. Pinto, M. N. Coelho Pinheiro, and J. B. L. M. Campos, "Coalescence of two gas slugs rising in a co-current flowing liquid in vertical tubes," Chem. Eng. Sci. **53**, 2973 (1998).
[21]T. S. Mayor, A. M. F. R. Pinto, and J. B. L. M. Campos, "Hydrodynamics of gas-liquid slug flow along vertical pipes in the laminar regime–experimental and simulation study," Ind. Eng. Chem. Res. **46**, 3794 (2007).
[22]J. R. Fagundes Netto, J. Fabre, and L. Peresson, "Bubble-bubble interaction in horizontal two-phase slug flow," J. Braz. Soc. Mech. Sci. **23**, 463 (2001).
[23]P. Grenier, "Evolution des longueurs de bouchons en écoulement intermittent horizontal," Ph.D. thesis, Institut National Polytechnique de Toulouse, 1997.
[24]W. Salman, A. Gavriilidis, and P. Angeli, "On the formation of Taylor bubbles in small tubes," Chem. Eng. Sci. **61**, 6653 (2006).
[25]E. Almatroushi and A. Borhan, "Interaction and coalescence of drops and bubbles rising through a tube," Ind. Eng. Chem. Res. **45**, 398 (2006).
[26]W. L. Olbricht and D. M. Kung, "The interaction and coalescence of liquid drops in flow through a capillary tube," J. Colloid Interface Sci. **120**, 229 (1987).
[27]R. W. Aul and W. L. Olbricht, "Coalescence of freely suspended liquid drops in flow through a small pore," J. Colloid Interface Sci. **145**, 478 (1991).
[28]K. D. Danov, D. S. Valkovska, and P. A. Kralchevsky, "Hydrodynamic instability and coalescence in trains of emulsion drops or gas bubbles moving through a narrow capillary," J. Colloid Interface Sci. **267**, 243 (2003).
[29]H. L. Goldsmith and S. G. Mason, "The flow of suspensions through tubes. II. Single large bubbles," J. Colloid Sci. **18**, 237 (1963).
[30]M. J. Martinez and K. S. Udell, "Boundary integral analysis of the creeping flow of long bubbles in capillaries," ASME J. Appl. Mech. **56**, 211 (1989).
[31]D. M. Campana, S. Ubal, M. D. Giavedoni, and F. A. Saita, "Stability of the steady motion of a liquid plug in a capillary tube," Ind. Eng. Chem. Res. **46**, 1803 (2007).
[32]S. Ubal, D. M. Campana, M. D. Giavedoni, and F. A. Saita, "Stability of the steady displacement of a liquid plug driven by a constant pressure difference along a prewetted capillary tube," Ind. Eng. Chem. Res. **47**, 6307 (2008).
[33]W. Sabisch, "Dreidimensionale numerische Simulation der Dynamik von aufsteigenden Einzelblasen und Blasenschwärmen mit einer Volume-of-Fluid-Methode," Ph.D. thesis, University Karlsruhe, 2000.
[34]B. Ghidersa, M. Wörner, and D. G. Cacuci, "Exploring the flow of immiscible fluids in a square mini-channel by direct numerical simulation," Chem. Eng. J. **101**, 285 (2004).
[35]M. Wörner, B. Ghidersa, M. Ilić, and D.G. Cacuci, "Volume-of-fluid method based numerical simulations of gas-liquid two-phase flow in confined geometries," La Houille Blanche **6**, 91 (2005).
[36]M. Wörner, B. Ghidersa, and A. Onea, "A model for the residence time distribution of bubble-train flow in a square mini-channel based on direct numerical simulation results," Int. J. Heat Fluid Flow **28**, 83 (2007).
[37]F. Özkan, M. Wörner, A. Wenka, and H. S. Soyhan, "Critical evaluation of CFD codes for interfacial simulation of bubble-train flow in a narrow channel," Int. J. Numer. Methods Fluids **55**, 537 (2007).
[38]Ö. Keskin, M. Wörner, T. Bauer, H. S. Soyhan, and R. Lange, "Validierte numerische Simulation der Taylor-Strömung im quadratischen Mini-Kanal," Chem.–Ing.–Tech. **80**, 1302 (2008).
[39]F. P. Bretherton, "The motion of long bubbles in tubes," J. Fluid Mech. **10**, 166 (1961).
[40]M. D. Giavedoni and F. A. Saita, "The axisymmetric and plane cases of a gas phase steadily displacing a Newtonian liquid: A simultaneous solution of the governing equations," Phys. Fluids **9**, 2420 (1997).
[41]D. Halpern and P. Gaver, "Boundary element analysis of the time-dependent motion of a semi-infinite bubble in a channel," J. Comput. Phys. **115**, 366 (1994).
[42]R. A. Johnson and A. Borhan, "Pressure-driven motion of surfactant-laden drops through cylindrical capillaries: Effects of surfactant solubility," J. Colloid Interface Sci. **261**, 529 (2003).
[43]R. S. Abiev, "Simulation of the slug flow of a gas-liquid system in capillaries," Theor. Found. Chem. Eng. **42**, 105 (2008).
[44]F. Fairbrother and A. E. Stubbs, "Studies in electro-endosmosis. Part IV. The bubble-tube method of measurement," J. Chem. Soc. **1**, 527 (1935).
[45]G. I. Taylor, "Deposition of a viscous fluid on the wall of a tube," J. Fluid Mech. **10**, 161 (1961).
[46]W. L. Chen, M. C. Twu, and C. Pan, "Gas-liquid two-phase flow in microchannels," Int. J. Multiphase Flow **28**, 1235 (2002).
[47]B. G. Cox, "An experimental investigation of the streamlines in viscous fluid expelled from a tube," J. Fluid Mech. **20**, 193 (1964).
[48]C.-H. Hsu, P.-C. Chen, K.-Y. Kung, and C. Lai, "Impacts of ratio of asymptotic bubble width to diameter of a circular tube and Reynolds number in a gas bubble driven flow," Chem. Eng. Sci. **60**, 5341 (2005).
[49]R. K. Shah and A. L. London, *Laminar Flow Forced Convection in Ducts* (Academic, New York, 1978), p. 198.
[50]T. C. Thulasidas, M. A. Abraham, and R. L. Cerro, "Flow patterns in liquid slugs during bubble-train flow inside capillaries," Chem. Eng. Sci. **52**, 2947 (1997).
[51]A. N. Tsoligkas, M. J. H. Simmons, and J. Wood, "Influence of orientation upon the hydrodynamics of gas-liquid flow for square channels in monolith supports," Chem. Eng. Sci. **62**, 4365 (2007).
[52]M. N. Kashid, I. Gerlach, S. Goetz, J. Franzke, J. F. Acker, F. Platte, D. W. Agar, and S. Turek, "Internal circulation within the liquid slugs of a liquid-liquid slug-flow capillary microreactor," Ind. Eng. Chem. Res. **44**, 5003 (2005).
[53]H. Fujioka and J. B. Grotberg, "Steady propagation of a liquid plug in a two-dimensional channel," J. Biomech. Eng. **126**, 567 (2004).
[54]N. Ashgriz and J. Y. Poo, "FLAIR: Flux line-segment model for advection and interface reconstruction," J. Comput. Phys. **93**, 449 (1991).
[55]H. Häfner, W. Schönauer, and R. Weiss, "The program package LINSOL: Basic concepts and realization," Appl. Numer. Math. **30**, 213 (1999).